THE JOURNAL OF BIOLOGICAL CHEMISTRY VOL. 285, NO. 28, pp. 21750–21767, July 9, 2010

Rab3-interacting Molecule γ Isoforms Lacking the Rab3-binding Domain Induce Long Lasting Currents but Block Neurotransmitter Vesicle Anchoring in Voltage-dependent P/Q-type Ca^{2+} Channels*[S]

Received for publication, January 6, 2010, and in revised form, April 27, 2010 Published, JBC Papers in Press, May 7, 2010, DOI 10.1074/jbc.M110.101311

Yoshitsugu Uriu[‡], Shigeki Kiyonaka[‡§], Takafumi Miki[‡], Masakuni Yagi[‡], Satoshi Akiyama[‡], Emiko Mori[‡], Akito Nakao[‡], Aaron M. Beedle[¶], Kevin P. Campbell[¶], Minoru Wakamori[‖], and Yasuo Mori[‡§1]

From the [‡]Department of Synthetic Chemistry and Biological Chemistry, Graduate School of Engineering, Kyoto University, Kyoto 615-8510, Japan, [§]Core Research for Evolution Science and Technology, Japan Science and Technology Agency, Chiyoda-ku, Tokyo 102-0075, Japan, the [¶]Howard Hughes Medical Institute and Departments of Molecular Physiology and Biophysics, Internal Medicine, and Neurology, University of Iowa Roy J. and Lucille A. Carver College of Medicine, Iowa City, Iowa 52242-1101, and the [‖]Department of Oral Biology, Graduate School of Dentistry, Tohoku University, Sendai 980-8575, Japan

Assembly of voltage-dependent Ca^{2+} channels (VDCCs) with their associated proteins regulates the coupling of VDCCs with upstream and downstream cellular events. Among the four isoforms of the Rab3-interacting molecule (RIM1 to -4), we have previously reported that VDCC β-subunits physically interact with the long α isoform of the presynaptic active zone scaffolding protein RIM1 (RIM1α) via its C terminus containing the C_2B domain. This interaction cooperates with RIM1α-Rab3 interaction to support neurotransmitter exocytosis by anchoring vesicles in the vicinity of VDCCs and by maintaining depolarization-triggered Ca^{2+} influx as a result of marked inhibition of voltage-dependent inactivation of VDCCs. However, physiological functions have not yet been elucidated for RIM3 and RIM4, which exist only as short γ isoforms (γ-RIMs), carrying the C-terminal C_2B domain common to RIMs but not the Rab3-binding region and other structural motifs present in the α-RIMs, including RIM1α. Here, we demonstrate that γ-RIMs also exert prominent suppression of VDCC inactivation via direct binding to β-subunits. In the pheochromocytoma PC12 cells, this common functional feature allows native RIMs to enhance acetylcholine secretion, whereas γ-RIMs are uniquely different from α-RIMs in blocking localization of neurotransmitter-containing vesicles near the plasma membrane. γ-RIMs as well as α-RIMs show wide distribution in central neurons, but knockdown of γ-RIMs attenuated glutamate release to a lesser extent than that of α-RIMs in cultured cerebellar neurons. The results suggest that sustained Ca^{2+} influx through suppression of VDCC inactivation by RIMs is a ubiquitous property of neurons, whereas the extent of vesicle anchoring to VDCCs at the plasma membrane may depend on the competition of α-RIMs with γ-RIMs for VDCC β-subunits.

Protein complexes play essential roles in various cellular responses including neurotransmission via synapses in the nervous system. In central synapses, the postsynaptic density is formed by protein complexes, containing neurotransmitter receptors, signaling, and cytoskeletal proteins, and scaffolding proteins, such as PSD-95 (1), whereas active zones are formed by the cytomatrix and other proteins responsible for neurotransmitter release from presynaptic nerve terminals (2–6). For Ca^{2+} influx upon membrane potential depolarization to evoke neurotransmitter release, efficient coupling of VDCCs[2] to protein machineries, such as soluble *N*-ethylmaleimide-sensitive factor attachment protein receptors (SNAREs), mediating fusion of neurotransmitter-containing vesicles with presynaptic membranes, is critical (7–13). Thus, it is extremely important to identify protein associations and their functional significance in understanding neurotransmission.

Multiple types of VDCCs are distinguished on the basis of biophysical and pharmacological properties (14). In neurons, high voltage-activated (HVA) VDCC types, such as the N-, P/Q-, R-, and L-types are essential for neurotransmitter release from presynaptic terminals (15–17). Furthermore, presynaptic Ca^{2+} channels were considered to serve as the regulatory node in a dynamic, multilayered signaling network that exerts short term control of neurotransmission in response to synaptic activity (13). Biochemically, VDCCs are known as heteromultimeric protein complexes composed of the pore-forming α_1 and auxiliary subunits α_2/δ, β, and γ (18). The α_1-subunit, designated as Ca_V, is encoded by 10 distinct genes, whose correspondence with functional subtypes has been largely elucidated

* This work was supported by research grants from the Ministry of Education, Culture, Sport, Science and Technology of Japan.
[S] The on-line version of this article (available at http://www.jbc.org) contains supplemental Tables S1–S5 and Figs. 1–6.
[1] To whom correspondence should be addressed: Dept. of Synthetic Chemistry and Biological Chemistry, Graduate School of Engineering, Kyoto University, Katsura campus, Nishikyo-ku, Kyoto 615-8510, Japan. Tel.: 81-75-383-2761; Fax: 81-75-383-2765; E-mail: mori@sbchem.kyoto-u.ac.jp.

[2] The abbreviations used are: VDCC, voltage-dependent calcium channel; SNARE, soluble *N*-ethylmaleimide-sensitive factor attachment protein receptor; CNS, central nervous system; RIM, Rab3-interacting molecule; RIM-BP, RIM-binding protein; DMEM, Dulbecco's modified Eagle's medium; WB, Western blotting; DIV, days *in vitro*; CSM, crude synaptic membranes; TIRF, total internal reflection fluorescence; HVA, high voltage-activated; RT, reverse transcription; GST, glutathione *S*-transferase; GFP, green fluorescent protein; DIG, digoxigenin; GAPDH, glyceraldehyde-3-phosphate dehydrogenase; NPY, neuropeptide Y; ACh, acetylcholine; HPLC, high pressure liquid chromatography; EGFP, enhanced GFP; shRNA, short hairpin RNA; siRNA, small interfering RNA; shControl, control shRNA; siControl, control siRNA.

(14, 18). VDCC complexes are primarily known for association with presynaptic and postsynaptic proteins, including syntaxin, SNAP-25, synaptotagmin, CASK, and Mint via interactions with the α_1-subunit (8, 9, 19–24). It was traditionally believed that the presence of anchoring Ca^{2+} channels close to the Ca^{2+} microdomain-dependent release machinery was the main reason for the physical interactions between channels and synaptic proteins. However, it is now becoming clear that these proteins additionally regulate channel activity. The β-subunit interacts with α_1 from the cytoplasmic side to enhance functional channel trafficking to the plasma membrane (25, 26) and to modify multiple kinetic properties (27, 28). Association with other proteins has also been revealed for β-subunits (12, 29–31). Considering the cytoplasmic disposition of β-subunits, it is intriguing to investigate whether β-subunits are involved in targeting specific subcellular machinery to VDCC complexes at presynaptic active zones for neurotransmitter release through as yet unidentified protein interactions.

Originally identified as a putative effector of the synaptic vesicle protein Rab3 (32), RIM1 is part of the RIM superfamily, whose members share a common C_2B domain at their C termini (33). With regard to RIM1 and RIM2, a long isoform α and short isoforms β and γ that lack the Rab3-interacting Zn^{2+} finger domain are known, whereas only short γ forms are known for RIM3 and RIM4 (33, 34). A recent paper (35) identified RIM3γ as a postsynaptic protein. RIM1 has been shown to interact with other presynaptic active zone protein components, including Munc13, ELKS (also known as CAST), RIM-binding protein (RIM-BP), and liprins, to form a protein scaffold in the presynaptic nerve terminal (2, 36–39). Recently, we reported that the association of RIM1 with β-subunits supports neurotransmitter release via two distinct mechanisms: sustaining Ca^{2+} influx through inhibition of channel inactivation and anchoring neurotransmitter-containing vesicles in the vicinity of VDCCs (12). Importantly, presynaptic VDCC currents manifest resistance to voltage-dependent inactivation and exhibit inactivation largely dependent upon the magnitude of the inward Ca^{2+} current (40, 41), as observed for VDCCs associated with RIM1 (12). Furthermore, we demonstrated that the mouse RIM1 arginine-to-histidine substitution (R655H), which corresponds to the human autosomal dominant cone-rod dystrophy mutation (42), modifies RIM1 function in regulating VDCC currents elicited by the P/Q-type $Ca_V2.1$ and L-type $Ca_V1.4$ channels (43).

Genetic studies using mouse knockouts have shown that RIM1 is essential for different forms of synaptic plasticity in different types of synapses (39, 44, 45). In the CA1 region Schaffer collateral excitatory synapses and GABAergic synapses, RIM1 maintains normal neurotransmitter release and short term synaptic plasticity. In excitatory CA3-region mossy fiber synapses, cerebellar parallel fiber synapses, and cortico-lateral amygdala synapses, RIM1 is necessary for presynaptic long term plasticity. Using pharmacological and genetic approaches, a presynaptic signaling pathway via cAMP, protein kinase A, and RIM1α was elucidated as a general mechanism that underlies the long term modulation of transmitter release at both excitatory and inhibitory synapses (46). In autapses, the RIM1α deletion significantly reduces the readily releasable pool of vesicles, and it alters short term plasticity and the properties of evoked asynchronous release (47). More recently, severe impairment of mouse survival by deletion of both RIM1α and RIM1β was reported (34). Electrophysiological analyses showed that the deletion of both RIM1α and RIM1β abolished long term presynaptic plasticity, as does RIM1α deletion alone, but aggravated the impairment in synaptic strength and short term synaptic plasticity that is caused by the RIM1α deletion. Mice deficient in both RIM1α and RIM2α showed lethality due to defects in Ca^{2+}-triggered release, despite normal presynaptic active zone length and normal spontaneous neurotransmitter release (48). In *Caenorhabditis elegans*, the loss of the single RIM homolog, UNC10, caused a reduction in membrane-contacting synaptic vesicles within 30 nm of the dense projection at neuromuscular junctions (49). In support of our hypothesis regarding VDCC-RIM1α association (12), a recent report states that RIM colocalizes with the Ca^{2+} channels and provides a mechanism to target vesicles to the presynaptic density through direct interaction with Rab3 at *C. elegans* presynaptic densities (50). However, despite this progress in genetic studies of RIMs, RIM2, RIM3, and RIM4 have yet to be characterized functionally (33, 35, 36, 51), and physiological roles played by RIM1 remain controversial (52).

Here, we analyze a physical and functional interaction between RIM family members and VDCC β-subunits. γ-RIMs as well as α-RIMs interact with four VDCC β-subunits and markedly suppress the voltage-dependent inactivation of P/Q-type $Ca_V2.1$ VDCC expressed in BHK cells, and are essential for regulation of Ca^{2+}-triggered exocytosis in PC12 cells and in cultured cerebellar neurons. Unlike α-RIMs, γ-RIMs suppress anchoring of neurotransmitter-containing vesicles to VDCCs.

EXPERIMENTAL PROCEDURES

cDNA Cloning and Construction of Expression Vectors—RIM1α (GenBank™ accession number NM_053270), RIM2α (GenBank™ accession number HM015529), RIM3γ (GenBank™ accession number NM_182929), and RIM4γ (GenBank™ accession number NM_183023) were cloned from mouse brain Marathon-Ready cDNA (Clontech) using PCR. Mouse brain RIM2α is a novel variant that is highly homologous with RIM2α (NM_053945) cloned from the rat brain. The amino acid sequence of mouse RIM2α is slightly different from rat RIM2α mainly in three regions (^{542}GDMEYSWLEHASWHSSEASPM-SL^{563} in rat RIM2α is replaced with ^{542}GDSQKGKRKTSEQG-VLSDSNTRSERQKKRMYYGGHSLEEDLEWSEPQIKDSGV-DTCSSTTLNEEHSHSDK^{611} in mouse brain RIM2α, and ^{733}SQSLSRRTTPFVPRVQ^{748} and ^{1132}MITEDMDSTRKRNS^{1145} in rat RIM2α are deleted in mouse brain RIM2α). These clones were subcloned into pCI-neo (Promega) and the FLAG-tagged vector pCMV-tag2 (Stratagene). Rat β_{4b} (GenBank™ accession number XM_215742) was subcloned into the same vectors.

Production of Glutathione S-Transferase (GST) Fusion Proteins and Recombinant β_4-Subunit Proteins—For production of GST fusion proteins for RIMs, each cDNA for RIM constructs and cDNA for GST were subcloned together into the pET23 vector (Novagen). The Rosetta strain (Novagen) of *Escherichia coli* was transformed by the expression vectors, and protein

expression/purification was performed according to the manufacturer's instructions (Novagen). For production of recombinant β_4-subunits, the gene encoding amino acid residues 47–475 of rat β_{4b}-subunit and cDNA for GST were subcloned into the pET23 vector (Novagen). The GST-β_4 fusion proteins were purified by glutathione-Sepharose beads (GE Healthcare), and the GST tag was cleaved by incubation with thrombin (4 units/ml; Sigma) for 6 h at 4 °C. Resultant GST and thrombin were removed by glutathione-Sepharose beads and by benzamidine beads (Sigma) to obtain purified recombinant β_4-subunits. These proteins were stored at −80 °C.

GST Pull-down Assay and Coimmunoprecipitation in HEK293T Cells—HEK293T cells were cultured in Dulbecco's modified Eagle's medium (DMEM) containing 10% fetal bovine serum, 30 units/ml penicillin, and 30 μg/ml streptomycin. Forty-eight h after transfection, HEK293T cells were solubilized in Nonidet P-40 buffer (150 mM NaCl, 50 mM Tris, 1% Nonidet P-40, and protease inhibitors) and then centrifuged at 17,400 × *g* for 20 min. For the pull-down assay, the cell lysate was incubated with glutathione-Sepharose beads bound with purified fusion proteins at 4 °C, and then the beads were washed with Nonidet P-40 buffer. The proteins retained on the beads were characterized by Western blot (WB) with anti-GFP antibody (Clontech catalog no. 632460). For coimmunoprecipitation, the cell lysate was incubated with anti-FLAG M2 monoclonal antibody (Sigma catalog no. F3165), and then the immunocomplexes were incubated with protein A-agarose beads (Santa Cruz Biotechnology, Inc., Santa Cruz, CA), and the beads were washed with Nonidet P-40 buffer. Immunoprecipitated proteins were characterized by WB with anti-β_4 antibody.

In Vitro Binding of the Purified RIM-GST Fusion Proteins and Recombinant β_4-Protein—RIM-GST fusion proteins at various concentrations were incubated with 50 pM purified recombinant β_4-subunits for 3 h at 4 °C in phosphate-buffered saline buffer containing 0.1% Nonidet P-40 and 50 μg/ml bovine serum albumin and then incubated with glutathione-Sepharose beads for 1 h. The beads were washed twice with the phosphate-buffered saline buffer. The proteins retained on the beads were characterized by WB with the anti-β_4 antibody (12) and detected by enhanced chemiluminescence (Thermo Scientific). The densities of protein signals, obtained using NIH Image under a linear relationship with the applied amount of proteins, were normalized to the densities from the maximal binding.

Cell Culture and cDNA Expression in BHK Cells—The baby hamster kidney BHK6-2 cell line stably expressing $Ca_V2.1$, α_2/δ, and β_{1a} was described previously (53). BHK6-2 cells were cultured in DMEM containing 10% fetal bovine serum, 30 units/ml penicillin, and 30 μg/ml streptomycin. Transfection of cDNA plasmids was carried out using Effecten transfection reagent (Qiagen). The cells were subjected to electrophysiological measurements 48 h after transfection.

Current Recordings—Whole-cell mode of the patch clamp technique was carried out at 22–25 °C with an EPC-9 (HEKA Elektronik) patch clamp amplifier as described previously (54). Patch pipettes were made from borosilicate glass capillaries (1.5-mm outer diameter, 0.87-mm inner diameter; Hilgenberg) using a model P-87 Flaming-Brown micropipette puller (Sutter Instrument Co.). The patch electrodes were fire-polished. Pipette resistance ranged from 2 to 3.5 megaohms when filled with the pipette solutions described below. The series resistance was electronically compensated to >60%, and both the leakage and the remaining capacitance were subtracted by the $-P/4$ method. Currents were sampled at 100 kHz after low pass filtering at 8.4 kHz (3 db) in the experiments of activation kinetics, otherwise sampled at 20 kHz after low pass filtering at 3.0 kHz (3 db). Data were collected and analyzed using Pulse version 8.77 (HEKA Elektronik). An external solution contained 3 mM $BaCl_2$, 155 mM tetraethylammonium chloride, 10 mM HEPES, and 10 mM glucose (pH 7.4-adjusted with TEA-OH) for BHK cells and 10 mM $BaCl_2$, 153 mM tetraethylammonium chloride, 10 mM HEPES, and 10 mM glucose (pH 7.4-adjusted with tetraethylammonium hydroxide) for PC12 cells. The pipette solution contained 95 mM CsOH, 95 mM aspartate, 40 mM CsCl, 4 mM $MgCl_2$, 5 mM EGTA, 2 mM disodium ATP, 5 mM HEPES, and 8 mM creatine phosphate (pH 7.2-adjusted with CsOH).

Voltage Dependence of Inactivation—To determine the voltage dependence of inactivation (inactivation curve) of VDCCs, Ba^{2+} currents were evoked by 20-ms test pulse to 5 mV after the 10-ms repolarization to −100 mV (−80 mV for PC12) following 2-s holding potential (V_h) displacement (conditioning pulse) from −100 to 20 mV (from −80 to 20 mV for PC12) with 10-mV increments. Amplitudes of currents elicited by the test pulses were normalized to those elicited by the test pulse after a 2-s V_h displacement to −100 mV (−80 mV for PC12). The mean values were plotted against potentials of the 2-s V_h displacement. When the inactivation curve was monophasic, the mean values were fitted to the single Boltzmann equation: $h(V_h) = (1 - a) + a/(1 + \exp((V_{0.5} - V_h)/k))$, where a is the rate of inactivating component, $V_{0.5}$ is the potential to give a half-value of inactivation, and k is the slope factor. Otherwise, the mean values were fitted to the sum of two Boltzmann equations: $h(V_h) = (1 - a - b) + a/(1 + \exp((V_{0.5}{}^{Low} - V_h)/k^{Low})) + b/(1 + \exp((V_{0.5}{}^{High} - V_h)/k^{High}))$, where a, b, and $(1 - a - b)$ are the ratios of a low voltage-induced phase, a high voltage-induced phase, and a non-inactivating phase; $V_{0.5}{}^{Low}$ and $V_{0.5}{}^{High}$ are the potentials that give a half-value of components susceptible to inactivation at low voltages in inactivation curves and at high voltages; and k^{Low} and k^{High} are the slope factors.

Voltage Dependence of Activation—Tail currents were elicited by repolarization to −60 mV after 5-ms test pulse from −40 to 30 mV with 5-mV increments. Currents were sampled at 100 kHz after low pass filtering at 8.4 kHz. Amplitudes of tail currents were normalized to the tail current amplitude obtained with a test pulse to 30 mV. The mean values were plotted against test pulse potentials and fitted to the Boltzmann equation: $n(V_m) = 1/(1 + \exp((V_{0.5} - V_m)/k))$, where V_m is membrane potential, $V_{0.5}$ is the potential to give a half-value of conductance, and k is the slope factor.

RNA Preparation, Northern Blot Analysis, and Real-time PCR—Total RNA was prepared from various tissues of 2-month-old C57BL/6 mice with ISOGEN total RNA isolation reagent (Nippon Gene) according to the manufacturer's instructions. For Northern blot analysis, 30 μg of total RNA was separated by electrophoresis in a denaturating gel and blotted onto nylon membrane (Roche Applied Science). The probes

used to detect RIM1 and RIM2 RNA were cDNA fragments corresponding to nucleotides 1035–1491 of mouse RIM1α and nucleotides 471–1372 of mouse RIM2α, respectively. The probes used to detect RIM3 and RIM4 were cDNA fragments corresponding to coding sequence of mouse RIM3γ and RIM4γ, respectively. The cDNA probes were labeled with digoxigenin (DIG) using the PCR DIG labeling kit (Roche Applied Science). The hybridization, washing, and detection were performed according to the manufacturer's instructions. Equal loading of total RNA was estimated by ethidium bromide staining of ribosomal RNAs.

For real-time PCR, reverse transcription of RNA to cDNA was performed using an RNA LA-PCR kit (TaKaRa). Quantification was performed by real-time PCR (LightCycler Instrument, Roche Applied Science) using the LightCycler FastStart DNA Master HybProbe Kit (Roche Applied Science). Primer sequences are indicated in supplemental Table S1. Temperature cycles were as follows. Initial 95 °C for 10 min was followed by 40 cycles at 95 °C for 10 s, 60 °C for 10 s, 72 °C for 30 s for RIM1; at 95 °C for 10 s, 60 °C for 10 s, 72 °C for 30 s for RIM2; at 95 °C for 10 s, 60 °C for 10 s, 72 °C for 30 s for RIM3; at 95 °C for 10 s, 60 °C for 10 s, 72 °C for 30 s for RIM4; and at 95 °C for 10 s, 57 °C for 5 s, 72 °C for 5 s for 18 S ribosomal RNA (18 S). The results were analyzed with LightCycler software. The identity of the PCR product was confirmed by automated determination of the melting temperature of the PCR products. The results for each gene were normalized relative to 18 S, as described previously (55), and were expressed relative to the brain given the arbitrary value of 1.

In Situ Hybridization Histochemistry—For histological staining of the central nervous system (CNS), adult mice (C57BL/6, body weight 20–25 g) were deeply anesthetized with an overdose of Nembutal and then transcardially perfused by 0.9% NaCl, followed by 3% paraformaldehyde in 0.1 M phosphate buffer (pH 7.4). The brains of the animals were dissected. Cryoprotection of the tissue blocks in 30% sucrose for 24 h at 4 °C was followed by histological sectioning on a cryostat (Leica). For details about *in situ* hybridization histochemistry, see Kagawa *et al.* (56). Briefly, *in vitro* transcribed DIG-labeled cRNA probe was generated against template RIM3γ or RIM4γ cDNA fragment corresponding to cording sequence of mouse RIM3γ or RIM4γ using DIG High Prime kit (Roche Applied Science). The probe (0.3 μg/ml) was hybridized overnight to mouse CNS histological 35-μm-thick sections at 50 °C. Positive signals were detected by alkaline phosphatase-conjugated anti-digoxigenin antibody and the nitro blue tetrazolium/5-bromo-4-chloro-3′-indolyl phosphate reaction.

Biochemistry of Native Neuronal VDCC Complexes—To obtain the crude synaptic membrane (CSM) fraction, subcellular fractionation was performed based on a previously described method (24), with slight modification. Whole mouse brains (8 g) were homogenized in a homogenization buffer containing 4 mM HEPES, 0.32 M sucrose, 5 mM EDTA, 5 mM EGTA, and protease inhibitors (pH 7.4). Cell debris and nuclei were removed by centrifugation at 800 × *g* for 10 min. The supernatant (S1) was centrifuged at 9,000 × *g* for 15 min to obtain crude synaptosomal fraction as pellet (P2). The supernatant was stored as S2. The crude synaptosomes were resuspended in the homogenization buffer and centrifuged at 10,000 × *g* for 15 min. The washed crude synaptosomes were lysed by hypoosmotic shock in water, rapidly adjusted to 1 mM HEPES/NaOH (pH 7.4), and stirred on ice for 30 min. After centrifugation of the lysate at 25,000 × *g* for 20 min, the pellet was resuspended in 0.25 M buffered sucrose. The synaptic membranes were then further enriched through a discontinuous sucrose gradient containing 0.8/1.0/1.2 M sucrose. After centrifugation at 65,000 × *g* for 2 h, the CSM fraction was collected from the 1.0/1.2 M sucrose interface. S1, P2, S2, and CSM fractions were analyzed by WB using rabbit anti-RIM1 polyclonal antibody raised against amino acid residues 11–399 of mouse RIM1, anti-RIM3 polyclonal antibody raised against the peptide containing GSQQAGGGAGTTTAKK, anti-PSD-95 monoclonal antibody (Thermo scientific catalog no. MA1-045), and anti-synaptophysin monoclonal antibody (Sigma catalog no. S5768).

Synaptic membrane proteins were extracted from the CSM with solubilization buffer containing 50 mM Tris, 500 mM NaCl, a mixture of protease inhibitors, and 1% digitonin (Biosynth) (pH 7.4). After centrifugation at 147,600 × *g* for 37 min, supernatant was diluted with a buffer containing 50 mM Tris and 1% digitonin to adjust NaCl concentration to 150 mM and incubated overnight at 4 °C. After centrifugation at 6,654 × *g* for 15 min, the supernatant was incubated with protein A-agarose coupled to anti-RIM1/2 antibody (Synaptic Systems catalog no. 140-203) or anti-RIM3 polyclonal antibody for 6 h at 4 °C. Immunoprecipitated proteins were subjected to WB with anti-$Ca_V2.1$ antibody (Alomone catalog no. ACC-001), anti-$Ca_V2.2$ antibody (Alomone catalog no. ACC-002), or anti-β_4 antibody.

PC12 Cell Culture and siRNA Suppression of Endogenous RIMs in PC12 Cells—PC12 cells were cultured as described previously (57). The siRNA sequences for rat RIM1 and RIM2 were described previously (12). The sense siRNA sequences 5′-AAGCTCCGAGGGCACGTTTAT-3′ and 5′-AACTGGCTGGTACAAACTCTT-3′ for RIM3 and 5′-AACTATGGAGGAGTTTGTCTA-3′ and 5′-AACTGCCAGCTGCCTATATCA-3′ for RIM4 were used. To construct siRNA oligomers, the Silencer siRNA construction kit (Ambion) was used. The GAPDH siRNA (siControl) used was the control provided with the kit. Transfection of siRNAs to PC12 cells was carried out using Lipofectamine™ 2000 (Invitrogen). Cells were transfected with combinations of 0.5 μg each of siRNAs in a 35-mm culture dish. Suppression of RNA expression was confirmed by reverse transcription (RT)-PCR analyses (29 cycles) using specific primers listed in supplemental Table S1 and WB analyses. RT-PCR was performed using the LA-PCR kit (TaKaRa), according to the manufacturer's instructions. The cells treated with siRNAs were subjected to WB analyses, patch-clamp measurements, imaging of secretory vesicles, or release assay 48 h after transfection. To generate expression vectors (pCI-neo) for siRNA-resistant RIMs (denoted by an asterisk), silent mutations were introduced in the siRNA-binding regions of RIM. Silent mutations of RIM1 were introduced by substituting the nucleotide sequence ^{4198}aga atg gac cac aaa tgc^{4217} for ^{4198}ag**g** atg ga**t** ca**t** aa**g** tg**t**^{4217} and ^{4267}gtg att gga tgg tat aaa^{4284} for ^{4267}gt**a** at**c** gg**c** tgg ta**c** aa**g**^{4284}. Silent mutations of RIM2 were introduced by substituting the nucleotide sequence ^{4429}gcc cag ata ctc tta gat^{4446} for ^{4429}gc**g** ca**a** at**c**

ct**t** tt**g** ga**c**^{4446} and ^{4453}gaa cta tcc aac^{4464} for ^{4453}ga**g** ct**t** tc**g** aa**t**^{4464}. Silent mutations of RIM3 were introduced by substituting the nucleotide sequence ^{346}agc tcc gag ggc acg ttt^{363} for ^{346}ag**t** tcc ga**a** gg**t** ac**a** tt**c**^{363} and ^{811}ggc tgg tac aaa^{822} for ^{811}gg**t** tgg ta**t** aa**g**^{822}. Silent mutations of RIM4 were introduced by substituting the nucleotide sequence ^{244}tat gga gga gtt tgt^{258} for ^{244}ta**c** gg**c** gg**c** gt**a** tg**c**^{258} and ^{445}ctg cca gct gcc tat atc^{462} for ^{445}ct**a** cc**t** gc**a** gc**t** ta**c** at**a**^{462}. Letters in boldface type indicate mutated nucleotides. In rescue experiments, rescue plasmids were cotransfected with siRNAs using Lipofectamine™ 2000. 1.0 μg each of siRNA-resistant RIM1* and RIM2* and/or 0.4 μg each of siRNA-resistant RIM3* and RIM4* were cotransfected with 0.5 μg each of siRNA in a 35-mm culture dish.

WB Analysis of PC12 Cells Transfected with siRNAs—PC12 cells transfected with siRNAs were solubilized and analyzed by WB using anti-$Ca_V2.1$ polyclonal antibody, anti-$Ca_V2.2$ polyclonal antibody, anti-β_3 antibody (Abcam catalog no. ab16717), anti-RIM1/2 polyclonal antibody, anti-RIM3 polyclonal antibody, anti-RIM4 polyclonal antibody (Santa Cruz Biotechnology, Inc., catalog no. sc-85885), anti-Munc13 monoclonal antibody, anti-synaptotagmin I monoclonal antibody (WAKO catalog no. 017-15761), anti-SNAP-25 monoclonal antibody (BD Transduction Laboratories catalog no. S35020), anti-syntaxin monoclonal antibody, and anti-Rab3 monoclonal antibody (BD Transduction Laboratories catalog no. 610379).

Total Internal Reflection Fluorescence (TIRF) Imaging of Secretory Vesicles—PC12 cells cotransfected with pVenus-N1-NPY carrying a DNA construct for the fusion protein of neuropeptide Y (NPY) and the fluorescent protein Venus (NPY-Venus) and a mixture of RIM siRNAs using OptiFect (Invitrogen) were plated onto poly-L-lysine-coated coverslips. The imaging was performed in modified Ringer's buffer that contained 130 mM NaCl, 3 mM KCl, 5 mM $CaCl_2$, 1.5 mM $MgCl_2$, 10 mM glucose, and 10 mM HEPES (pH 7.4). Fluorescence images of NPY-Venus in large dense core vesicles were observed as previously reported (12, 58). In brief, a high numerical aperture objective lens (Plan Apochromatic, ×100, numerical aperture = 1.45, infinity-corrected, Olympus) was mounted on an inverted microscope (IX71, Olympus), and incident light for total internal reflection illumination was introduced from the high numerical objective lens through a single mode optical fiber. A diode-pumped solid state 488-nm laser (kyma488, 20 milliwatts, MELLES GRIOT) was used for total internal fluorescence illumination, and a 510-nm long pass filter was used as an emission filter. Images were captured by a cooled CCD camera (EM-CCD, Hamamatsu Photonics) operated with Metamorph (Molecular Devices). Densities of vesicles were assessed by counting the number of individual fluorescent spots in the area where vesicles show uniform distribution in TIRF images, and obtained numbers were divided by areas. Area calculations were performed using Metamorph software. The cells with distribution of vesicles by a dark spot with area of >10 μm^2 were omitted, to select the cells in which vesicles were uniformly distributed for the analyses. Ten μm^2 was adopted because 10 μm^2 was the maximal dark circle area that can be located in between vesicles in the images from siRIM1&2-transfected cells with uniform vesicle distribution.

Release Assay in PC12 Cells—Acetylcholine (ACh) secretion experiments were performed as previously reported with slight modifications (57). PC12 cells were plated in poly-D-lysine-coated 35-mm dishes (BD Biosciences) with 5×10^5 cells/dish. Cells were cotransfected with 5 μg of each RIM plasmid and 1 μg of pEFmChAT encoding mouse ChAT cDNA using Lipofectamine™ 2000. Three days after transfection, PC12 cells were washed with a 5.9 mM K^+ solution that contained 0.01 mM eserine, 140 mM NaCl, 4.7 mM KCl, 1.2 mM KH_2PO_4, 2.5 mM $CaCl_2$, 1.2 mM $MgSO_4$, 11 mM glucose, and 15 mM HEPES (pH 7.4-adjusted with NaOH) and incubated for 30 s with the 5.9 mM K^+ solution at 37 °C. The release of ACh during this period was considered as basal release. To measure K^+-stimulated release of ACh, the cells were then incubated for 30 s with a 51.1 mM K^+ solution that contained 0.01 mM eserine, 94.8 mM NaCl, 49.9 mM KCl, 1.2 mM KH_2PO_4, 2.5 mM $CaCl_2$, 1.2 mM $MgSO_4$, 11 mM glucose, and 15 mM HEPES (pH 7.4-adjusted with NaOH) or for 2 min with a 28.4 mM K^+ solution that contained 0.01 mM eserine, 94.8 mM NaCl, 27.2 mM KCl, 1.2 mM KH_2PO_4, 2.5 mM $CaCl_2$, 1.2 mM $MgSO_4$, 11 mM glucose, and 15 mM HEPES (pH 7.4-adjusted with NaOH). Supernatant from cells solubilized in Nonidet P-40 buffer and centrifuged at 17,400 × *g* for 20 min at 4 °C was taken as the cellular ACh that was not secreted. ACh was measured using HPLC with electrochemical detection (HTEC-500, EiCOM).

Fluorescent $[Ca^{2+}]_i$ Measurements—PC12 cells cotransfected with pEGFP-N1 and mixture of RIM siRNAs using Opti-Fect (Invitrogen). Thirty-six h after transfection, PC12 cells were plated onto poly-L-lysine-coated glass coverslips. Forty-eight h after transfection, cells on coverslips were loaded with fura-2 by incubation in DMEM containing 10 μM fura-2/AM (Dojindo Laboratories), 0.04% Pluronic F-127 (Biotium), and 10% fetal bovine serum at 37 °C for 40 min and washed with the 5.9 mM K^+ solution. The coverslips were then placed in a perfusion chamber mounted on the stage of the microscope. Fluorescence images of the cells were recorded and analyzed with a video image analysis system (AQUACOSMOS, Hamamatsu Photonics). The fura-2 fluorescence at an emission wavelength of 510 nm was observed at 37 ± 1 °C by exciting fura-2 alternately at 340 and 380 nm. Measurement was carried out in 5.9 mM K^+ solution, 51.1 mM K^+ solution, and 28.4 mM K^+ solution. The 340:380 nm ratio images were obtained on a pixel by pixel basis and were converted to Ca^{2+} concentrations by *in vivo* calibration using 40 μM ionomycin (59).

Construction of Short Hairpin RNA (shRNA) Vectors—shRNA vectors were constructed based upon a pSUPER.neo+GFP vector (OligoEngine). To create shRIM2, shRIM3, and shRIM4, two complementary 60-bp oligonucleotides carrying antisense and sense sequence for GGCCCAGATACTCTTAGAT (19 bp corresponding to nucleotides 4554–4572 of rat RIM2), CTGGCTGGTACAAATTCTT (nucleotides 1252–1270 of rat RIM3), and CTGCCAGCTGCCTATATCA (nucleotides 445–463 of rat RIM4) were annealed and ligated to pSUPER.neo+GFP vectors in accordance with the Oligo-Engine instructions. To create shRIM1, 60-bp oligonucleotides carrying GTAATAAATGAAGAGGTTTAAACTTCTTCGTTTGTTGC and its complementary sequence were annealed and ligated to pSUPER.neo+GFP vectors. In construction of

shRIM1, we inserted a mutation in the stem sequence of shRNA according to the previous report (60) for better silencing efficiency. Control shRNA (shControl) was generated similarly except that an artificial 19-mer sequence (ATCCGCGCGATAGTACGTA) was used as a target. This sequence was based upon a commercially available negative control siRNA sequence (B-Bridge International), and we confirmed that it had no significant identity to any known mammalian gene based on a BLAST search.

Rat Cerebellar Neuron Primary Cultures and Transfection—Primary cerebellar neuron cultures were prepared as previously described (61) with minor modifications. Briefly, cerebella from 7–9-day-old Wister rat pups were digested with 1% trypsin (Difco). The solution was removed after a brief centrifugation, and the tissue was mechanically dissociated by repeated pipetting in DMEM containing 10% fetal calf serum (Invitrogen). The cell suspension was centrifuged at 200 × *g* for 3 min. The pellet was resuspended in DMEM containing 10% fetal calf serum and filtered through a 70-μm cell strainer. After centrifugation at 100 × *g* for 5 min, 5×10^6 cells were resuspended in 100 μl of rat neuron nucleofector solution (Amaxa) with 3 μg of shRNA vector (total amount of DNA was 4 μg in all cases). The cell suspension was electroporated using the G-13 program (Amaxa). The cells were diluted with DMEM containing 10% fetal calf serum and seeded onto a polyethyleneimine-coated 15-mm diameter 4-well multidish (Nunc) at a density of 1×10^6 cells/well. Two h after initial plating, the medium was removed and gently replaced with Neurobasal medium containing 0.5 mM glutamine, 26 mM KCl, 60 units/ml penicillin, 60 μg/ml streptomycin, and 2% B-27 (Invitrogen). The cultures were maintained at 37 °C with 5% CO_2. The medium was very gently replaced with fresh medium every 3 days.

Glutamate Release Assay—After the transfection with shRNA vectors, cerebellar neurons (10 days *in vitro* (DIV)) were washed briefly with prewarmed low K^+ solution that contained 140 mM NaCl, 4.7 mM KCl, 1.2 mM KH_2PO_4, 2.5 mM $CaCl_2$, 1.2 mM $MgSO_4$, 11 mM glucose, and 15 mM HEPES-NaOH (pH 7.4) and were incubated for 1 min with the low K^+ solution at 37 °C. The release of glutamate during this period was considered as basal release. To measure K^+-stimulated release of glutamate, the cells were then incubated for 1 min with a high K^+ solution that contained 94.8 mM NaCl, 49.9 mM KCl, 1.2 mM KH_2PO_4, 2.5 mM $CaCl_2$, 1.2 mM $MgSO_4$, 11 mM glucose, 15 mM HEPES-NaOH (pH 7.4). Glutamate was determined by reverse-phase HPLC on an Eicompak SC-5ODS (EiCOM), using precolumn derivatization with *o*-phthalaldehyde and electrochemical detection (HTEC-500, EiCOM).

Statistical Analysis—All data accumulated under each condition from at least three independent experiments are expressed as means ± S.E. Student's *t* test or analysis of variance followed by Fisher's test was employed.

RESULTS

Direct Interaction of RIMs with VDCC β-Subunits—The C-terminal sequence of RIM1 (RIM1α(1231–1463)) that interacts with VDCCs is highly conserved among RIM family members (83, 73, and 65% identity with RIM2α(1339–1572), RIM3γ(77–307), and RIM4γ(36–269), respectively) (Fig. 1*A*). We first tested the ability of RIM proteins to bind to the β-subunits of VDCCs. To test the importance of the conserved C terminus, direct protein-protein interactions between RIMs (RIM1α(1079–1463), RIM2α(1193–1572), RIM3γ, and RIM4γ) and VDCC β-subunits (β_{1a}, β_{2a}, β_3, and β_{4b}) were examined by *in vitro* pull-down assays. GST fusion RIM proteins (Fig. 1*A*) immobilized on glutathione-Sepharose beads were incubated with cell lysate obtained from HEK293T cells transfected with each EGFP-tagged β-subunit. Bound proteins analyzed by WB using anti-GFP antibody revealed that the respective RIM isoforms bind to four VDCC β-subunit isoforms (Fig. 1*B*). To compare the affinity of binding to RIM3γ among VDCC β-subunits, amounts of β-proteins bound to GST-RIM3γ were quantified and normalized to those of input β-subunits. The relative amounts of β-subunits pulled down by GST-RIM3γ suggested that RIM3γ has a higher binding affinity to β_3 and β_{4b}, the brain-type β-subunits (62, 63), compared with the skeletal and cardiac muscle-type β-subunits, β_{1a} and β_{2a} (64, 65) (Fig. 1*C*). Subsequent *in vitro* binding assays using purified preparation of recombinant β_4-subunit (amino acid residues 47–475) and GST-RIM proteins revealed a dissociation constant (K_d) of 39.3 ± 3.9 nM ($n = 4$) for RIM2α(1193–1572), which was similar to that for RIM1α(1079–1463) (35.1 nM) (adapted from Kiyonaka *et al.* (12)), whereas the K_d values for RIM3γ (233 ± 57 nM, $n = 4$) and RIM4γ (566 ± 63 nM, $n = 3$) were almost an order of magnitude higher than those of α-RIMs (Fig. 1*D*). Furthermore, coimmunoprecipitation experiments revealed an association between recombinant VDCC β_{4b}-subunit and FLAG-tagged RIMs in HEK293T cells (Fig. 1*E* and supplemental Fig. 1). RIM1α and RIM2α were more efficiently coimmunoprecipitated with the β_{4b}-subunit compared with RIM3γ and RIM4γ, which is consistent with the results of the GST pull-down assays. These results suggest that γ-RIMs directly interact with VDCC β-subunits with a lower binding affinity than those of α-RIMs.

Functional Effects of RIMs on P/Q-type VDCC Currents—To elucidate the functional significance of the direct interaction between RIMs and VDCC β-subunits, we examined whole-cell Ba^{2+} currents through recombinant P/Q-type VDCCs expressed as $\alpha_1 \cdot \alpha_2/\delta \cdot \beta$ complexes containing the BI-2 variant of $Ca_V2.1$ (25) and β_{1a} in BHK cells. Prominent effects of RIMs on P/Q-type VDCC currents were observed for the parameters of voltage-dependent inactivation. Inactivation was markedly decelerated (Fig. 2*A*), whereas the voltage dependence of the inactivation was significantly shifted toward depolarizing potentials by RIMs: the inactivation curve showed a component susceptible to inactivation at high voltages (the half-inactivation potentials ($V_{0.5}$) ranged from −28 to −23 mV) and a non-inactivating component (Fig. 2*B* and supplemental Table S2). Furthermore, we coexpressed BADN, a dominant negative suppressor β_{4b} fusion construct designed to disrupt the association of β-binding proteins, such as RIMs, with the functional VDCC complex without interfering with the α_1-β interaction (12). BADN significantly diminished the effect of RIMs on P/Q channel inactivation. The inactivation kinetics were markedly accelerated, and biphasic inactivation curves were elicited (Fig. 2). In the presence of BADN, we observed components susceptible to inactivation at low voltages in inactivation curves ($V_{0.5}$ values

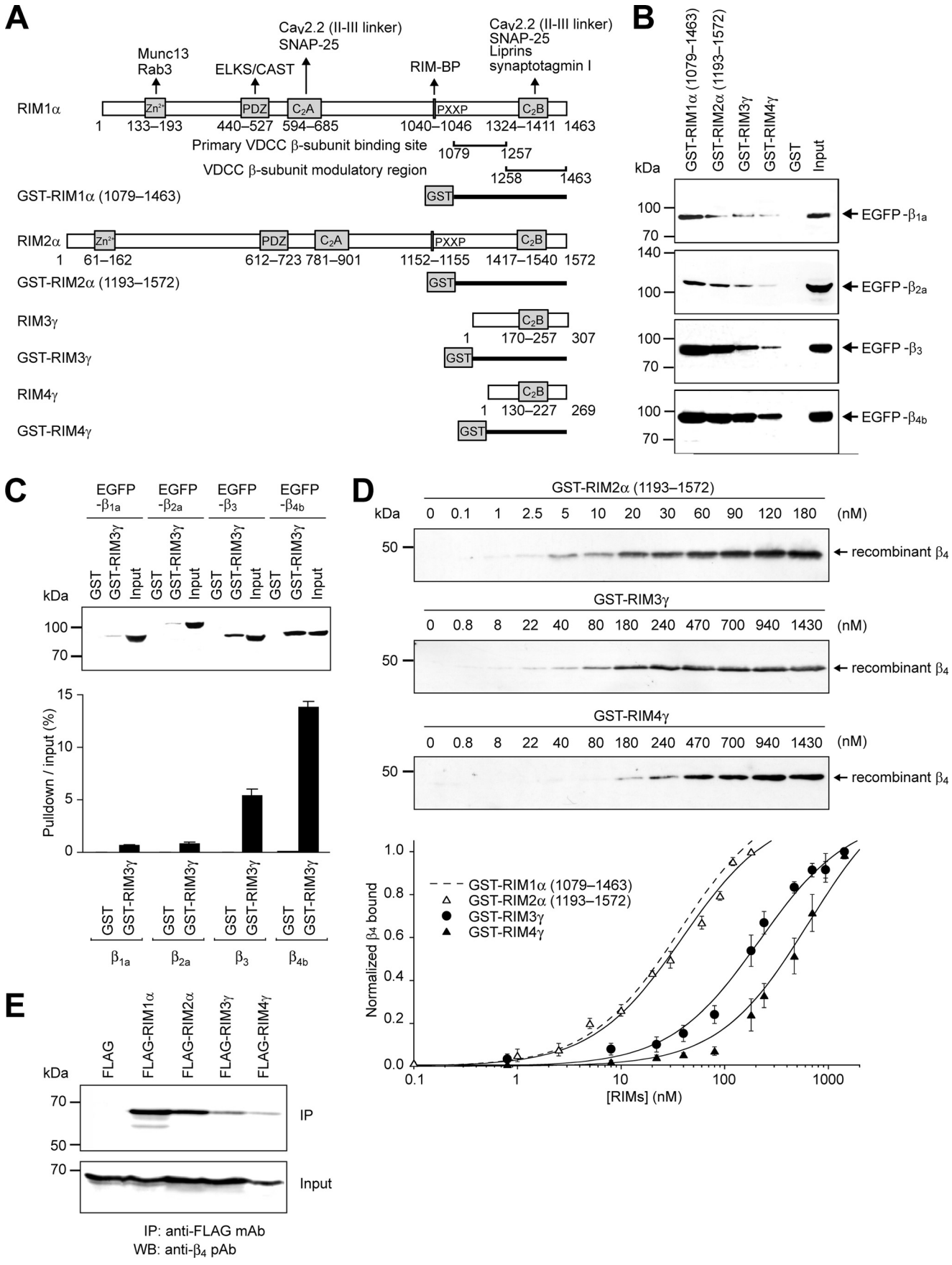

ranged from −72 to −63 mV) and at high voltages ($V_{0.5}$ values ranged from −27 to −19 mV) (Fig. 2*B* and supplemental Table S2). Thus, the strong suppressive effect on voltage-dependent inactivation of P/Q-type VDCCs via interaction with β-subunits is a functional feature common to RIMs.

RIM proteins differently modulated the activation kinetics of P/Q-type VDCCs (Fig. 3*A*). The time constant ($\tau_{activation}$) obtained by fitting the activation time course of inward currents with a single exponential was "bell-shaped" when plotted against different voltages. Activation showed the slowest speed at −15 mV in vector-, RIM1α-, and RIM2α-expressing cells and at −10 mV in RIM3γ- and RIM4γ-expressing cells. γ-RIMs significantly decelerated the activation kinetics at membrane potentials over −10 mV, whereas RIM1α only slightly decelerated the activation at membrane potentials over 10 mV, and RIM2α had no significant effect (Fig. 3*A* and supplemental Table S3). RIMs failed to exert effects on other functional parameters, such as the voltage dependence of activation and the current densities at different voltages (Fig. 3, *B* and *C*, and supplemental Table S3). Thus, γ-RIMs more significantly affect P/Q-type VDCC currents in terms of activation kinetics compared with α-RIMs.

Tissue Distribution of RIM3 and RIM4 Expression—RNA preparations from different mouse tissues and brain regions were subjected to Northern blot analyses using cDNA probes specific for RIM1, RIM2, RIM3, or RIM4 (Fig. 4*A*). RIM1 RNA was detected abundantly in the brain and at low levels in the eye. In the brain, RIM1 RNA was most abundant in the cerebrum and cerebellum. The principal transcripts of RIM2 (~7.0 and ~5.5 kb) were detected at a high level in the brain and eye and at lower levels in the kidney and testis. In the brain, RIM2 RNA transcripts were detected at the highest level in the cerebellum. RIM3 RNA was also detected at the highest level in the brain. In the brain, RIM3 RNA was detected at similar levels in the cerebrum, cerebellum, brainstem, and olfactory bulb. RIM4 RNA was also detected at the highest level in the brain. In the brain, RIM4 RNA was detected ubiquitously but at relatively low levels in the brainstem and olfactory bulb. Thus, compared with the relatively selective expression of RIM1 and RIM2, RIM3 and RIM4 are more widely distributed in the brain.

To quantify levels of expression, RNA preparations from different mouse tissues were subjected to real-time PCR analyses using RIM1-, RIM2-, RIM3-, and RIM4-specific primers (Fig. 4*B* and supplemental Table S1). The brain was a tissue with high levels of expression common to all RIMs. This is consistent with Northern blot analysis (Fig. 4*A*). Other tissues of high expression were the testis for RIM2, RIM3, and RIM4 and the eye for RIM2. Moderate levels of expression (>10% of the level in the brain) were observed in the dorsal root ganglion, eye, stomach, large intestine, and testis for RIM1; in the dorsal root ganglion, stomach, small intestine, large intestine, kidney, and ovary for RIM2; in almost all tested tissues except for the stomach and small intestine for RIM3; and in the eye, heart, thymus, and ovary for RIM4.

To determine exactly which cell types express RIM3 and RIM4 mRNA in the CNS, sections of 8-week-old C57BL/6 mouse brains were subjected to *in situ* hybridization histochemistry using cRNA probes specific for RIM3 or RIM4. RIM3 and RIM4 RNAs were expressed in neurons throughout the CNS, supporting the widespread distribution of RIM3 and RIM4 (Fig. 5*A*). For both RIM3 and RIM4, regions rich in glial cells (*e.g.* the white matter of the cerebral cortex and cerebellum) were not significantly labeled (Fig. 5, *A* (*a*) and *B* (*a*)). In the hippocampus, pyramidal neurons of the CA1-CA3 region, granule cells of the dentate gyrus, and interneurons exhibited positive labeling for RIM3 and RIM4 (Fig. 5, *A* (*b*) and *B* (*b*)). In the neocortex, stainings for RIM3 and RIM4 were more intense in layers III and IV of the neocortex in comparison with that in layers II, V, and VI (Fig. 5, *A* (*c*) and *B* (*c*)). In the thalamus, staining for RIM3 was relatively strong (Fig. 5*A* (*d*)), whereas RIM4 hybridization was relatively weak (Fig. 5*B* (*d*)). These results support our Northern blotting data indicating a relatively lower expression of RIM4 in the brainstem (Fig. 4*A*). In the cerebellar cortex, prominent RIM3 and RIM4 hybridization signals were observed in the granule and Purkinje cell layers (Fig. 5, *A* (*e*) and *B* (*e*)). The RIM3 distribution, which was consistent with a recent report (35), is similar to the expression pattern of RIM4 in the mouse brain except in the brainstem.

α-RIM and RIM3 Physically Associate with Native VDCCs in the Crude Synaptic Membrane from the Mouse Brain—Subcellular fractionation analysis of the mouse brain showed that RIM1 and RIM3 were highly concentrated in the CSM fraction, which was similar to that for PSD-95 and synaptophysin, established marker proteins of the postsynapse and presynapse, respectively (Fig. 6*A*). In immunoprecipitation analysis of the CSM fraction solubilized with 1% digitonin-containing buffer, the P/Q-type ($Ca_V2.1$) and N-type ($Ca_V2.2$) VDCC α_1-subunits and the VDCC β_4-subunit were coimmunoprecipitated with α-RIM (RIM1 or RIM2) and RIM3 (Fig. 6*B*). Thus, the P/Q-type and N-type channels are physically associated with RIM3 as well as with α-RIM in the CSM fraction of the mouse brain.

Physiological Relevance of RIM Effects on the Inactivation Properties of VDCCs—To investigate the physiological roles of RIM·β-subunit complexes in native systems, expression of RIM

FIGURE 1. **Direct interaction of RIMs with VDCC β-subunits.** *A*, domain structures and GST fusion constructs of mouse RIMs. The *arrows* indicate molecules interacting with RIM1 at the following domains: Zn^{2+} finger-like domain (*Zn^{2+}*), PDZ domain (*PDZ*), first and second C_2 domains (C_2A and C_2B), and proline-rich region (*PXXP*). Primary VDCC β-subunit binding site (RIM1α(1079–1257)) and VDCC β-subunit modulatory region (RIM1α(1258–1463)) are indicated according to Ref. 12. *B*, pull-down assay of β-subunits with GST fusion RIM constructs. GST fusion proteins immobilized on glutathione-Sepharose beads were incubated with cell lysates obtained from EGFP-β-transfected HEK293T cells. Bound proteins were analyzed by WB using antibody for GFP. *C*, a comparison of RIM3γ binding affinity among VDCC β-subunits. *Top*, β-subunits were analyzed by GST pull-down using GST- or GST-RIM3γ-coated beads. Input is 10% of the amount used for pull-down. *Bottom*, quantification of pull-down results (mean ± S.E. (*error bars*) of three experiments). *D*, *in vitro* association between the purified GST-RIM fusion constructs and recombinant β_4-subunit (amino acid residues 47–475). GST-RIM proteins at various concentrations, incubated with β_4 (50 pM), were captured by glutathione-Sepharose beads. Captured β_4-proteins were examined by WB. The *lower panel* shows the quantitative densitometric analysis of bands shown in the *upper panels*. The saturation curves were subjected to the nonlinear least squares curve-fitting method to evaluate the apparent K_d. The saturation curves for GST-RIM1α(1079–1463) were adapted from Kiyonaka *et al.* (12). *E*, interactions of recombinant β_{4b} and RIMs in HEK293T cells. The interactions were evaluated by immunoprecipitation (*IP*) with antibody for FLAG, followed by WB with antibody for β_4.

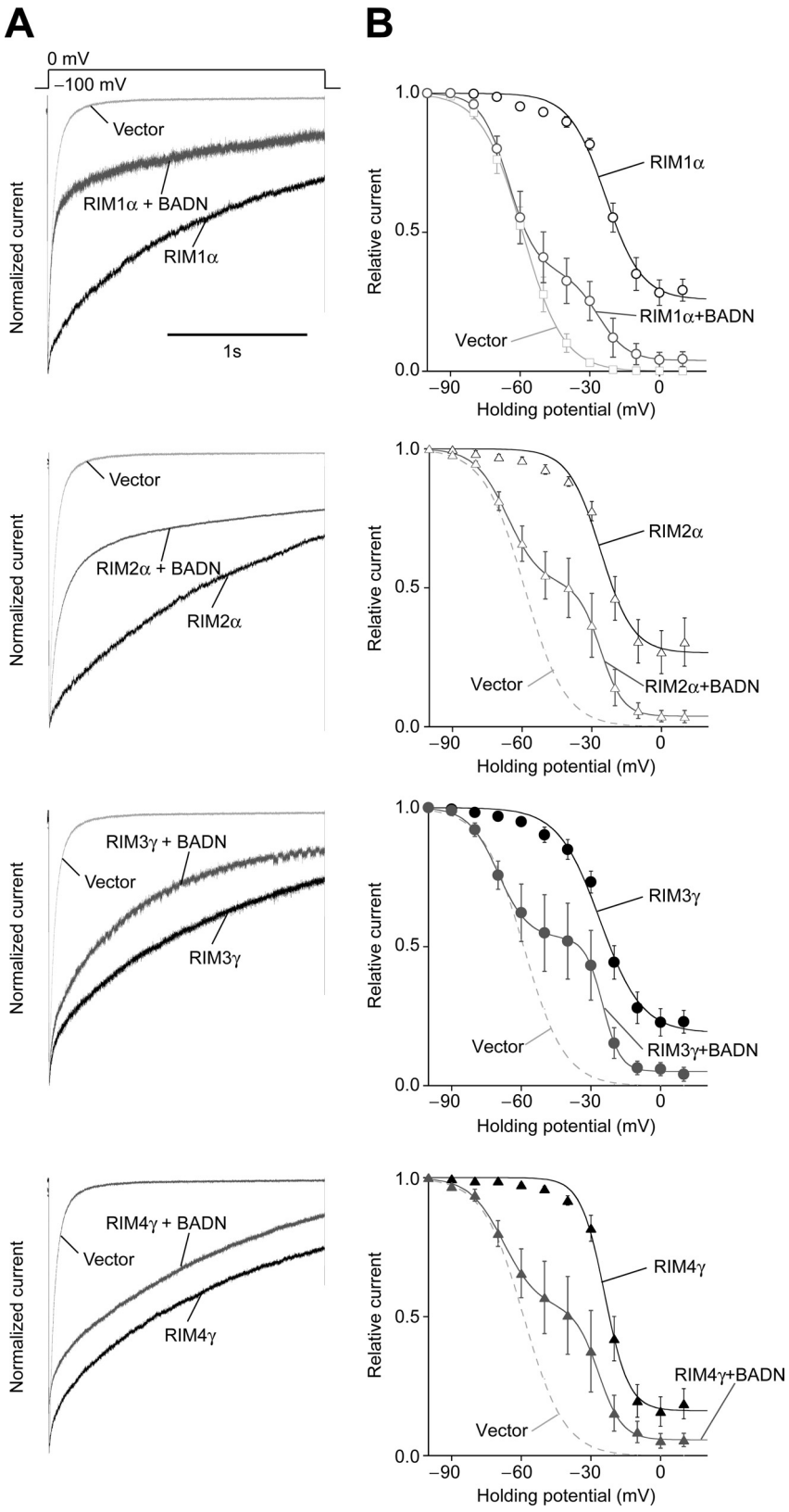

FIGURE 2. **Effects of RIMs on the inactivation properties of P/Q-type $Ca_V2.1$ channels.** *A*, effects of RIMs and BADN on inactivation of P/Q-type $Ca_V2.1$ currents in BHK cells expressing α_2/δ and β_{1a}-subunit. The peak amplitudes are normalized for Ba^{2+} currents elicited by 2-s pulses to 0 mV from a V_h of −100 mV. *B*, effects of RIMs and BADN on voltage dependence of inactivation of $Ca_V2.1$. To determine the voltage dependence of inactivation, currents were evoked by a 20-ms test pulse to 5 mV after the 10-ms repolarization to −100 mV following 2-s V_h displacements (conditioning pulses) from −100 to 20 mV with 10-mV increments. See supplemental Table S2 for statistical significance of the differences. *Error bars*, S.E.

was suppressed by treatment with siRNA (Fig. 7). In rat neuron-like pheochromocytoma PC12 cells, diverse HVA VDCC types have been precisely characterized (66, 67). Previously, we identified P/Q-, N-, and L-type Ca^{2+} currents by pharmacological dissection of HVA Ca^{2+} current and detected α_1 mRNA species (P/Q-type ($Ca_V2.1$), N-type ($Ca_V2.2$), and L-type ($Ca_V1.2$ and $Ca_V1.3$)) and β-subunits (β_1, β_2, and β_3) in PC12 cells (12). RT-PCR analysis revealed expression of RNA species encoding RIM1, RIM2, RIM3, and RIM4 in PC12 cells (Fig. 7*A*). RT-PCR analysis also showed that combinations of siRNAs specific for RIM1 and RIM2 (siRIM1&2), RIM3 and RIM4 (siRIM3&4), or all four RIMs (siRIM1&2&3&4) effectively suppressed the expression of target genes, whereas control siRNA (siControl) failed to exert significant effects on RIM RNA expression (Fig. 7*A*). WB also indicated that application of siRNAs for RIMs effectively suppressed expressions of RIM proteins (Fig. 7*B*). siRNAs for RIMs accelerated inactivation of whole-cell Ba^{2+} currents through VDCCs endogenously expressed in PC12 cells (Fig. 7*C*, *top*). The voltage dependence of VDCC inactivation in PC12 cells consisted of three phases: a low voltage-induced phase, a high voltage-induced phase, and a non-inactivating phase (Fig. 7*C* (*bottom*) and supplemental Table S4). siRNA application increased the proportion of the low voltage-induced phases (from 0.21 to 0.35 for siRIM1&2, to 0.38 for siRIM3&4, and to 0.46 for siRIM1&2&3&4) and reduced the proportion of the non-inactivating phases (from 0.42 to 0.30 for siRIM1&2, to 0.26 for siRIM3&4, and to 0.17 for siRIM1&2&3&4) (Fig. 7*C* (*bottom*) and supplemental Table S4). siRIM1&2&3&4 showed a more marked effect than siRIM1&2 or siRIM3&4. These inactivation properties were rescued by siRNA-resistant RIM constructs. Expression of siRNA-resistant (denoted by an asterisk) RIM

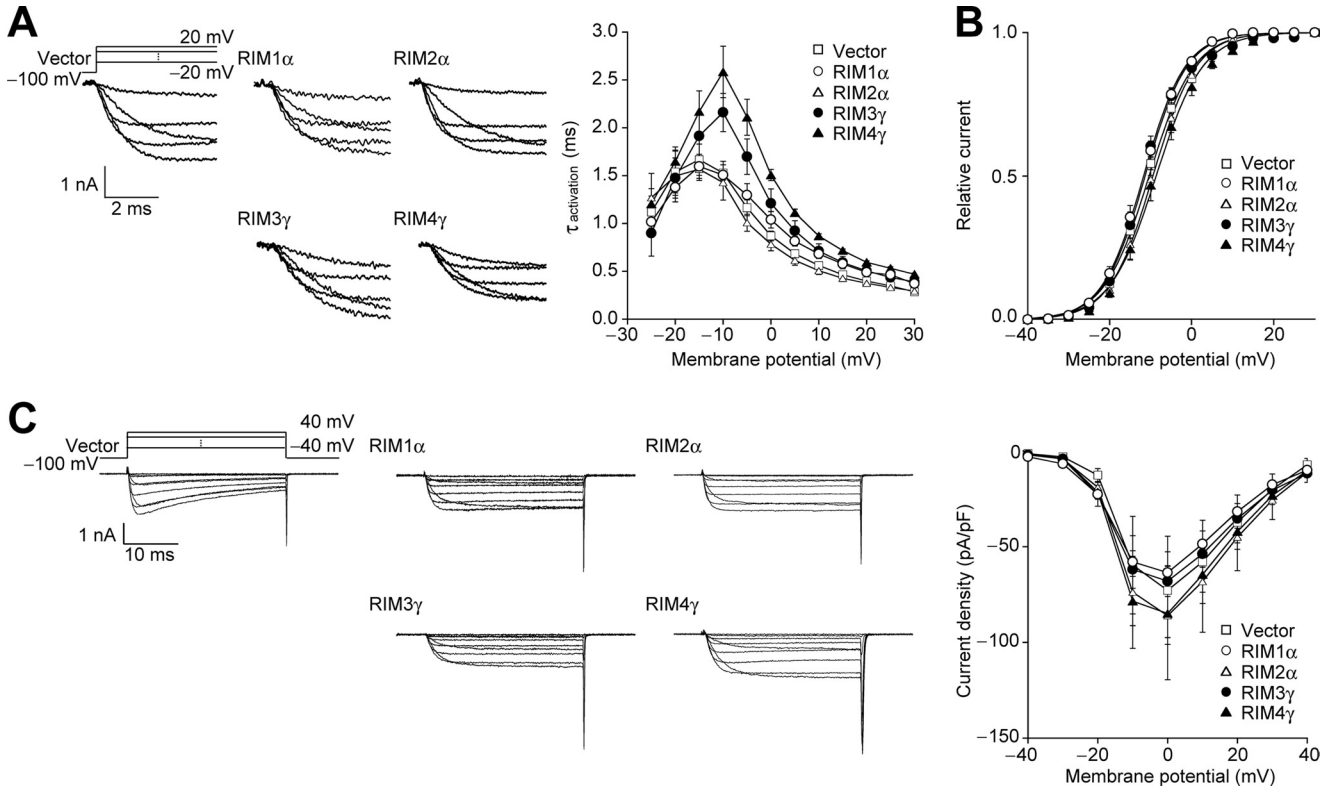

FIGURE 3. **Effects of RIMs on the activation properties of P/Q-type $Ca_V2.1$.** *A*, activation kinetics of P/Q-type $Ca_V2.1$ currents in BHK cells expressing α_2/δ- and β_{1a}-subunit. *Left*, families of representative Ba^{2+} currents. Currents evoked by 5-ms step depolarization from −20 to 20 mV in 10-mV increments from a V_h of −100 mV are displayed. *Right*, activation time constants plotted as a function of test potential. The activation phases are well fitted by a single exponential function at all potentials. Activation time constants ($\tau_{activation}$) were obtained from currents elicited by 5-ms step depolarization from −25 to 30 mV in 5-mV increments from a V_h of −100 mV. *B*, activation curves of P/Q-type $Ca_V2.1$ currents. Tail currents elicited by repolarization to −60 mV after 5-ms test pulses from −40 to 30 mV were used to determine activation curves. *C*, effects of RIMs on P/Q-type $Ca_V2.1$ currents. *Left*, representative traces for Ba^{2+} currents on application of test pluses from −40 to 40 mV with 10-mV increments from a V_h of −100 mV. *Right*, current density-voltage (*I-V*) relationships of $Ca_V2.1$. See supplemental Table S3 for statistical significance of the differences. *Error bars*, S.E.

cDNAs reversed the accelerated inactivation in RIM knockdown cells (siRIM1&2 + RIM1*&2* and siRIM3&4 + RIM3*&4*) (Fig. 7*C*, *middle*). The increase of the ratios of low voltage-induced phases and the reduction of ratios of non-inactivating phases were also rescued by the siRNA-resistant RIMs (0.05 and 0.41 for siRIM1&2 + RIM1*&2*; 0.12 and 0.42 for siRIM3&4 + RIM3*&4*). Other functional current parameters, such as current densities and activation kinetics at different voltages, were unaffected by siRNA for RIMs (supplemental Fig. 2 and Table S5). Thus, RIMs exert suppressive effects on voltage-dependent inactivation of native VDCCs in PC12 cells.

γ-RIMs Inhibit but α-RIMs Support Anchoring of Neurotransmitter Vesicles to VDCCs—Dense core vesicles were identified by a fusion protein of NPY and the fluorescent protein Venus (NPY-Venus) in PC12 cells. When cotransfected NPY-Venus was used as an siRNA transfection marker, comparison of fluorescence intensities of immunoreactivities to anti-RIM1 and RIM2 antibodies in NPY-Venus-positive PC12 cells with those in NPY-Venus-negative PC12 cells revealed that combination of specific siRNAs efficiently suppressed RIM1 and RIM2 expression in confocal images (supplemental Fig. 3). We directly observed fluorescent images in the plasma membrane area using evanescent wave microscopy, which illuminates only the subcellular area from the surface to a depth of less than 100 nm by TIRF. When cotransfected Ds-Red monomer was used as an siRNA transfection marker, comparison of fluorescence intensities of immunoreactivities to anti-RIM1 and RIM2 antibodies in Ds-Red-positive PC12 cells with those in Ds-Red-negative PC12 cells also revealed that combination of specific siRNAs efficiently suppressed RIM1 and RIM2 expression in TIRF images (supplemental Fig. 4). The number of vesicles docked to the plasma membrane was decreased significantly by combinatory application of RIM1 and RIM2 siRNAs, whereas it was increased by RIM3 and RIM4 siRNA (Fig. 8). Importantly, the inhibitory effect of siRIM1&2 and the enhancing effect of siRIM3&4 were reversed by expression of siRNA-resistant RIM cDNAs (siRIM1&2 + RIM1*&2* and siRIM3&4 + RIM3*&4*). Effects of siRIM1&2 or siRIM3&4 are unlikely to be due to altered densities of VDCCs at the plasma membrane in PC12 cells because the siRNAs used did not affect VDCC current densities and VDCC expression levels (Fig. 7*B* and supplemental Fig. 2*A* and Table S5). It is important to note that endogenous Rab3 and Munc13 were immunoprecipitated with FLAG-tagged α-RIMs but not γ-RIMs, whereas Liprin1-α was immunoprecipitated with α-RIMs and γ-RIMs (supplemental Fig. 6). This is consistent with the previous report that α-RIMs are associated with Rab3 and Munc13 via their N termini and with Liprin1-α via their C termini (32, 37, 39). Thus, γ-RIMs as well as α-RIMs play important roles in regulating neurotransmitter vesicle anchoring to VDCCs.

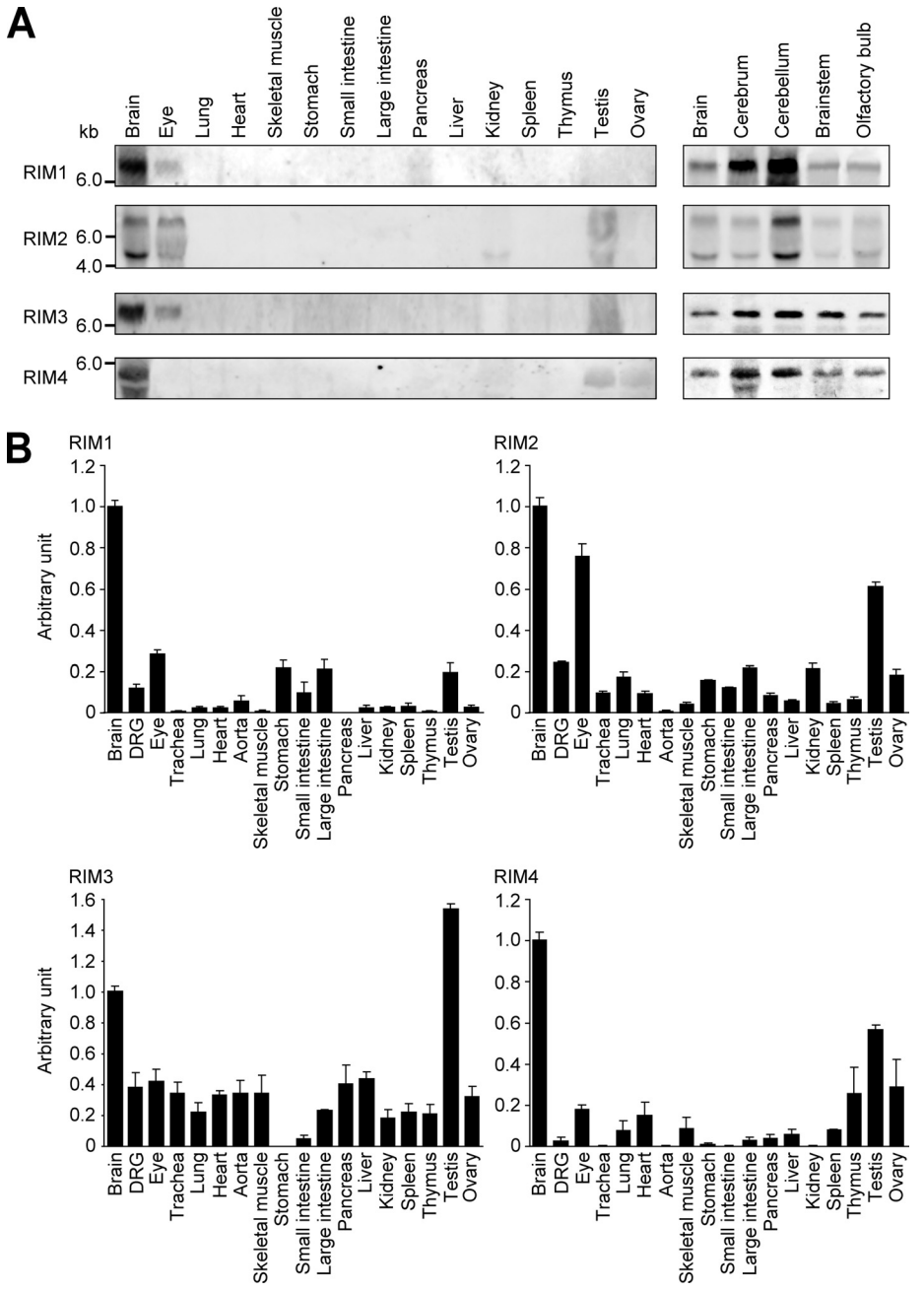

FIGURE 4. **Tissue distribution of RIMs.** *A*, Northern blot analyses show the tissue distribution of RIM1, RIM2, RIM3, and RIM4 RNAs. Positions of molecular size markers are identified on the *left*. *B*, real-time PCR analyses of the tissue distribution of RIM1, RIM2, RIM3, and RIM4 RNAs. The expression levels of RIM RNAs are normalized to those of 18 S. The results are expressed relative to the brain given the arbitrary value of 1 and are means ± S.E. (*error bars*) of at least three independent experiments.

γ-RIMs Enhance Neurotransmitter Secretion Less Potently than α-RIMs in PC12 Cells—We studied the physiological relevance of RIM interactions with the VDCC complexes by assessing neurotransmitter release from PC12 cells. PC12 cells were transfected with RIM cDNAs or with siRNAs for RIMs along with *Chat*, encoding choline acetyltransferase, which synthesizes ACh for synaptic vesicles (57). ACh release, triggered by Ca^{2+} influx in response to high K^+-induced (extracellular K^+ concentration elevated from 5.9 to 51.1 mM for 30 s) membrane depolarization, was less potently potentiated by recombinant RIM3γ and RIM4γ than by recombinant RIM1α and RIM2α (Fig. 9*A*). A similar result has been reported previously for RIM3γ for the secretion of human growth hormone in PC12 cells (36). siRNAs specific to RIMs significantly decreased ACh release. siRIM1&2&3&4 suppressed ACh secretion more markedly than siRIM1&2 or siRIM3&4. Furthermore, ACh release was abolished in the presence of 0.3 mM Cd^{2+}, a selective blocker of HVA Ca^{2+} channels, in extracellular solutions (Fig. 9*B*). Likewise, ACh release triggered by moderate depolarization (extracellular K^+ concentration elevated from 5.9 to 28.4 mM for 2 min) was also significantly decreased by siRNAs specific to RIMs (Fig. 9*C*). The inhibitory effects of siRIM1&2 and siRIM3&4 on depolarization-induced ACh release were rescued by expression of siRNA-resistant RIM cDNAs (Fig. 9, *B* and *C*). Notably, ACh release triggered by 28.4 mM K^+ was more susceptible to suppression by siRIM1&2 than by siRIM3&4. The amount of control ACh secretion by 51.1 mM K^+ solution nearly doubled that by 28.4 mM K^+ solution. The $[Ca^{2+}]_i$ under stimulation with extracellular K^+ elevation was estimated with fluorescent measurement using fura-2. In 51.1 and 28.4 mM K^+-containing extracellular solution, $[Ca^{2+}]_i$ elevations ($\Delta[Ca^{2+}]_i$) were observed and effectively decreased by knockdown of RIMs (Fig. 9, *D* and *E*). Control $[Ca^{2+}]_i$ elevation in 51.1 mM K^+ solution was approximately 1 order of magnitude higher than those in 28.4 mM K^+ solution. It is important to note that inhibition of ACh secretion by RIM siRNAs is unlikely to be due to their secondary effects that cause a mislocalization or reduction of the release machinery in PC12 cells because the siRNAs used did not affect the localization of syntaxin (supplemental Fig. 5) or the expression levels of essential components of the release machinery, such as synaptotagmin, SNAP-25, syntaxin, and Rab3 (Fig. 7*B*). Munc13 was slightly decreased in RIM1 and RIM2 knockdown cells (Fig. 7*B*), as reported in the RIM1 knock-out mouse, presumably because Munc13 binds to α-RIMs (supplemental Fig. 6) (37) and is destabilized in their absence (39). Thus, native γ-RIMs together with α-RIMs play important roles in neurotransmitter release in the PC12 cells.

γ-RIMs Support Neurotransmitter Secretion in Rat Cerebellar Neurons—To investigate physiological roles of RIMs in neurons, we next examined neurotransmitter release from cultured cerebellar neurons. RT-PCR analyses revealed expression of RNA species encoding RIM1, RIM2, RIM3, and RIM4 in cultured rat cerebellar neurons (Fig. 10*A*). Combinations of shRNAs specific for RIM1 and RIM2 (shRIM1&2), RIM3 and RIM4 (shRIM3&4), or four RIM isoforms (shRIM1&2&3&4) effectively suppressed the expression of target genes, whereas shControl failed to exert significant effects on RIM RNA expression in rat cerebellar neurons 10 days after transfection (Fig. 10*A*). Glutamate release from cerebellar neurons, triggered by Ca^{2+} influx in response to high K^+-induced (extracellular K^+ concentration elevated from 5.9 to 51.1 mM for 60 s) membrane depolarization, was significantly decreased by shRIM1&2, shRIM3&4, and shRIM1&2&3&4 (Fig. 10*B*). Notably, knockdown of α-RIMs (shRIM1&2) more markedly reduced glutamate release than that of γ-RIMs (shRIM3&4) and that of all RIMs (shRIM1&2&3&4). These results suggest that both α-RIMs and γ-RIMs are important for neurotransmitter release, but their contributions to glutamate release from cultured cerebellar neurons are different.

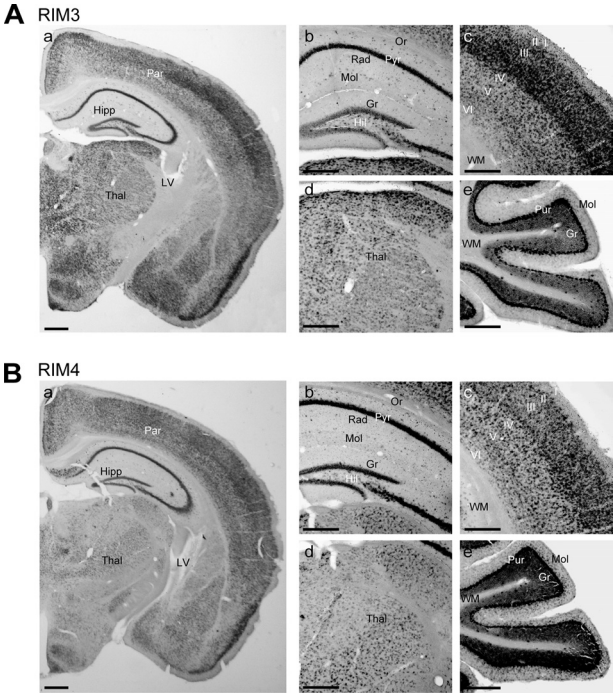

FIGURE 5. **Distribution of RIM3 and RIM4 RNA in the brain.** *In situ* hybridization photomicrographs show expression of RIM3 (*A*) and RIM4 (*B*) RNA in the forebrain (*A* (*a*) and *B* (*a*)), hippocampal formation (*A* (*b*) and *B* (*b*)), cerebral cortex (*A* (*c*) and *B* (*c*)), thalamus (*A* (*d*) and *B* (*d*)), and cerebellar cortex (*A* (*e*) and *B* (*e*)). *I–VI*, layers of cerebral cortex; *Gr*, granule cell layer of dentate gyrus (*A* (*b*) and *B* (*b*)) or cerebellar cortex (*A* (*e*) and *B* (*e*)); *Hil*, hilar region of hippocampal formation; *Hipp*, hippocampus; *LV*, lateral ventricle; *Mol*, stratum lacunosum-moleculare of hippocampal CA1 (*A* (*b*) and *B* (*b*)) or molecular cell layer of cerebellar cortex (*A* (*e*) and *B* (*e*)); *Or*, stratum orien; *Par*, parietal cortex; *Pyr*, stratum pyramidale; *Rad*, stratum radiatum; *Thal*, thalamus; *WM*, white matter. *Scale bars*, 500 μm in *A* (*a*) and *B* (*a*); 50 μm in *A* (*b–e*) and *B* (*b–e*).

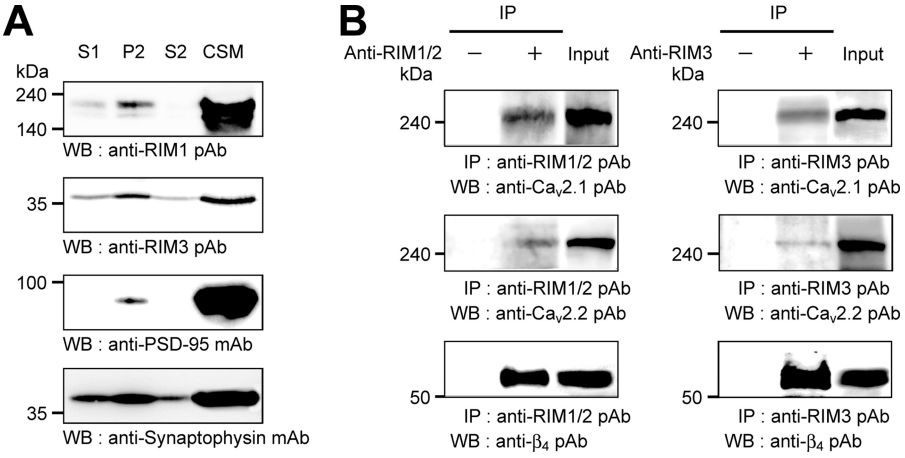

FIGURE 6. **Association of RIMs with native neuronal VDCC complexes in CSM fraction.** *A*, subcellular fractionation. The homogenate of mouse brain was subjected to subcellular fractionation. An aliquot of each fraction (10 μg of protein each) was analyzed by WB with the indicated antibodies. *S1*, crude synaptosomal fraction; *P2*, crude membrane fraction; *S2*, cytosolic synaptosomal fraction; *CSM*, CSM fraction. *B*, coimmunoprecipitation of RIMs with the VDCC subunits. Immunoprecipitation (*IP*) using an antibody for RIMs and subsequent WB for $Ca_V2.1$, $Ca_V2.2$, and β_4 was carried out on the CSM fraction.

DISCUSSION

An understanding of the physiological roles played by RIMs other than RIM1 has been elusive, despite evolutionary conservation of the C_2B domain-containing C terminus among all RIM isoforms. The present investigation revealed physical associations of RIM2α, RIM3γ, and RIM4γ with VDCC β-subunits. *In vitro* binding assays and coimmunoprecipitation experiments identified protein complexes formed by direct interactions of VDCC β-subunits with α_1-subunits and with RIMs (Figs. 1 and 6). The interactions between RIMs and VDCC β-subunits decelerated VDCC inactivation to sustain depolarization-induced Ca^{2+} influx (Figs. 2, 7, and 9, *D* and *E*) and enhanced depolarization-induced ACh release in PC12 cells (Fig. 9). TIRF imaging of dense core vesicles indicated that, unlike RIM1α and RIM2α, RIM3γ and RIM4γ inhibit the anchoring of neurotransmitter vesicles in the vicinity of VDCCs (Fig. 8).

K_d values of the binding of RIM1α(1079–1463), RIM2α(1193–1572), RIM3γ, and RIM4γ to the β_4-subunit indicate that the binding affinities of RIM3γ and RIM4γ are almost an order of magnitude lower than those of RIM1α and RIM2α (12) (Fig. 1*D*). This is consistent with the fact that the amino acid sequence of the primary β-subunit interaction region in the RIM1α (RIM1α(1079–1257)) (12) is better conserved in RIM2α (60% identity in RIM2α(1193–1366)) than in RIM3γ and RIM4γ (25 and 12% identities for RIM3γ(1–104) and RIM4γ(1–63), respectively). Despite these differences in affinity among the primary interaction regions for β-subunits, kinetic modulation of VDCC inactivation was observed for RIM3γ and RIM4γ as well as for RIM2α. This functional conservation in terms of VDCC regulation may be mainly attributable to the modulatory region (12) well conserved among all RIM proteins;

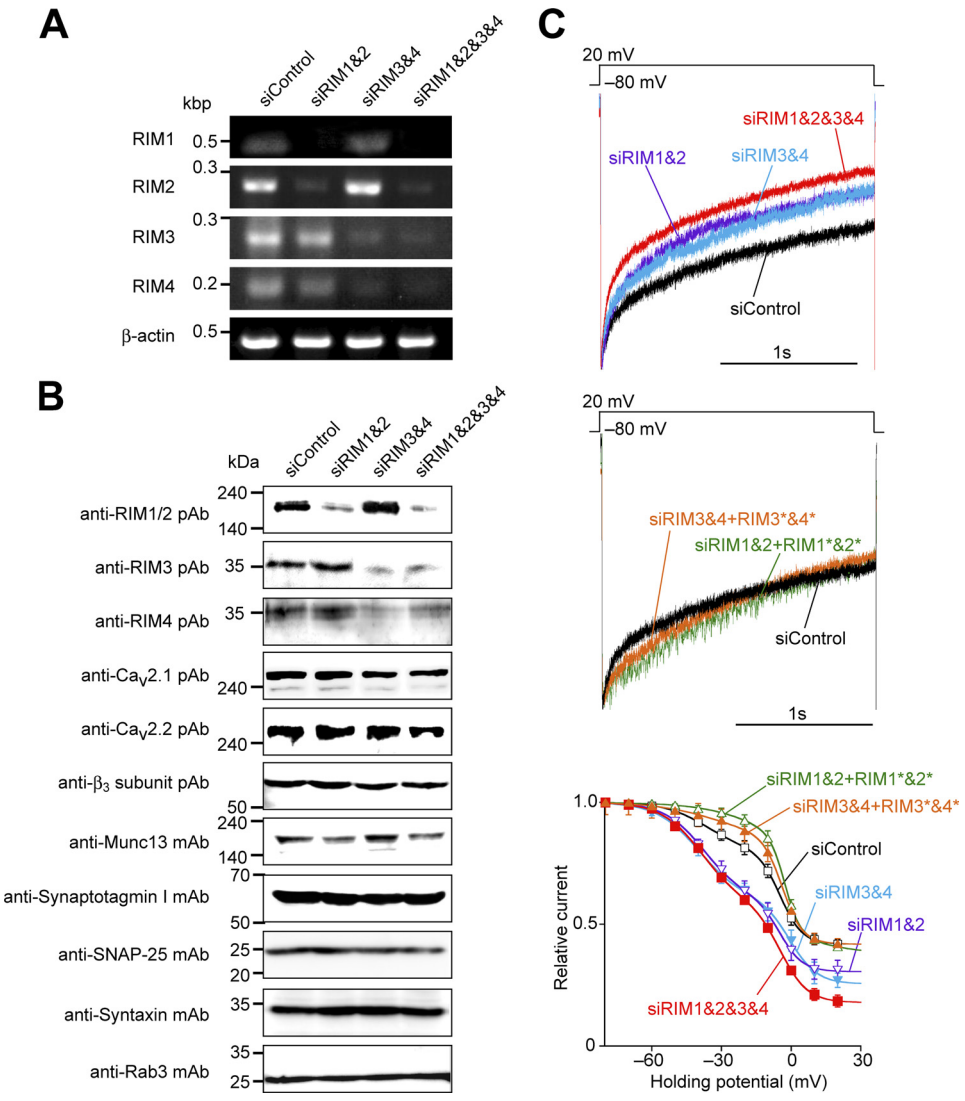

FIGURE 7. **Physiological relevance of effects of RIMs on inactivation properties of VDCCs.** *A*, RT-PCR analysis of RIM1, RIM2, RIM3, and RIM4 RNA expression in PC12 cells treated with GAPDH siRNA (*siControl*), a combination of RIM1- and RIM2-specific siRNAs (*siRIM1&2*), a combination of RIM3- and RIM4-specific siRNAs (*siRIM3&4*), and a combination of RIM1-, RIM2-, RIM3-, and RIM4-specific siRNAs (*siRIM1&2&3&4*). PCR was performed for 29 cycles. β-Actin was used as an internal control. *B*, WB of essential components of release machinery and VDCC subunits in PC12 cells transfected with the indicated combination of siRNAs. Primary antibodies used are indicated on the *left*. *C*, acceleration of inactivation by application of siRNAs specific for RIMs in VDCC currents recorded from PC12 cells. The acceleration of inactivation in RIM knockdown cells was reversed by expression of siRNA-resistant RIM cDNAs (siRIM1&2 + RIM1*&2*, and siRIM3&4 + RIM3*&4*). *Top* and *middle*, normalized current traces. *Bottom*, inactivation curves. See supplemental Table S4 for statistical significance of the differences.

identities with the RIM1α modulatory region (residues 1258–1463) (Fig. 1*A*) are 84, 74, and 67% for RIM2α(1367–1572), RIM3γ(105–307), and RIM4γ(64–269), respectively.

Although expression of RIM3γ or RIM4γ significantly inhibits its inactivation and slows the activation kinetics of recombinant P/Q-type VDCCs in BHK cells, knockdown of endogenous RIM3 and RIM4 promotes inactivation but fails to affect the activation kinetics of native VDCC currents in PC12 cells. In the recombinant BHK cell system, the P/Q-type formed by the $Ca_V2.1$ α_1- and β_{1a}-subunit was the only VDCC type expressed. However, PC12 cells express various VDCC subunits (the P/Q-, N-, and L-type α_1-subunits and the β_1-, β_2-, and β_3-subunits) (12, 66, 67). It is therefore possible that multiple types of VDCCs formed by various α_1- and β-subunits are regulated in a different manner by γ-RIMs in PC12 cells in terms of parameters such as activation. In fact, we previously reported, using the recombinant system, that RIM1α modulates VDCC activation properties, such as current density, voltage dependence of activation, and activation kinetics, depending on the subunit combination of the VDCC complex (12). In contrast to these functional parameters, similar RIM1α suppression of inactivation was observed for P/Q-type VDCCs containing a β_{2a}-, β_3-, or β_{4b}-subunit (12). Furthermore, a similar effect on inactivation by RIM1α was shown in N-type ($Ca_V2.2$), R-type ($Ca_V2.3$), and L-type ($Ca_V1.2$) VDCCs containing a β_{4b}-subunit. Thus, considering that the other β-subunits interact with RIMs even more strongly than β_{1a} (Fig. 1, *B* and *C*), suppressive effects of RIMs on inactivation are universal among HVA types, whereas effects of RIMs on activation kinetics are variable, depending on the subunit combination of the VDCC complex. Since the submission of this manuscript, similar modulation of $Ca_V1.3$ VDCC inactivation has been most recently reported for RIM2 (68).

Previous reports have demonstrated functional impacts of syntaxin, SNAP-25, and synaptotagmin on VDCCs through their physical association with the "synprint" region in the II-III linker of α_1-proteins (9, 19, 22). It has also been reported that RIM1 and RIM2 associate with the synprint (38, 69) directly via the C_2A domain and with the α_1 C-terminal tail indirectly via the RIM-BP (70) (Fig. 1*A*). However, inhibition of VDCC inactivation by RIMs may be independent of the synprint- or RIM-BP-mediated association because γ-RIMs, which lack both the C_2A domain necessary for synprint binding (38, 69) and the P*XX*P motif for the RIM-BP binding, inhibit VDCC inactivation (Fig. 2). This idea is supported by our observation that BADN was sufficient to inhibit the effects of RIMs on inactivation (Fig. 2). In addition, we have observed that replacement of β with the C-terminal truncation construct β_4-GK (71), which directly interacts with α_1 but lacks the ability to bind RIM1, was also sufficient to disrupt the RIM1 effects on inactivation (12). In our previous paper (12), we speculated that RIM1α may affect a conformational transition to the inactivated state of VDCCs via association with the β-subunit.

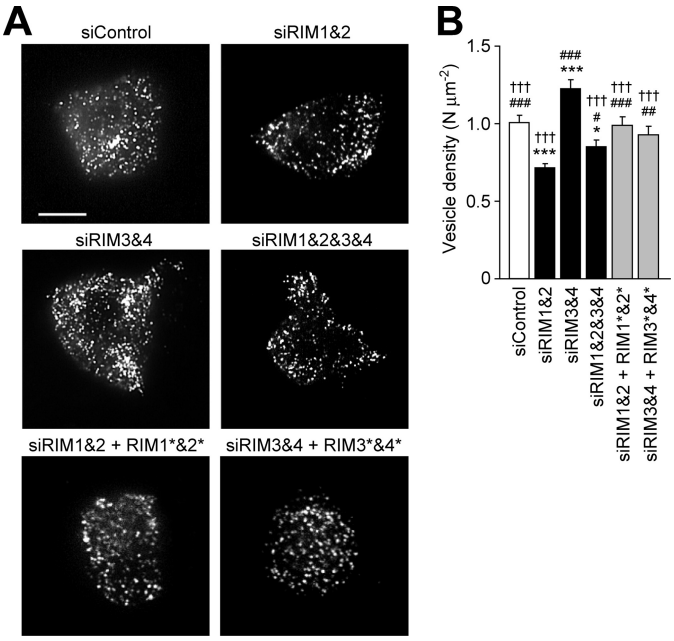

FIGURE 8. **γ-RIMs reduce the density of vesicles at the plasma membrane in PC12 cells.** *A*, typical TIRF images of plasma membrane-docked vesicles containing NPY-Venus are shown. NPY-Venus and combinations of siRNAs and siRNA-resistant RIM cDNAs were cotransfected in PC12 cells, and live images of cells were obtained by TIRF microscopy. *Scale bar*, 10 μm. *B*, the vesicle density (number (*N*) μm^{-2}) was determined by counting the vesicles in each image. The number of individual fluorescent spots in the area, where vesicles uniformly distributed in TIRF images, was divided by the area. Numbers of PC12 cells analyzed were 48, 51, 40, 45, 30, and 29 for transfection of siControl, siRIM1&2, siRIM3&4, siRIM1&2&3&4, siRIM1&2 + RIM1*&2*, and siRIM3&4 + RIM3*&4*, respectively. *, $p < 0.05$; ***, $p < 0.001$ *versus* siControl. #, $p < 0.05$; ##, $p < 0.01$; and ###, $p < 0.001$ *versus* siRIM1&2. †††, $p < 0.001$ *versus* siRIM3&4. *Error bars*, S.E.

Recently, it has been proposed that the HOOK domain, between the conserved Src homology 3 and guanylate kinase domains of the β-subunit, is an important determinant of inactivation (72). Hence, RIMs may act on the HOOK domain to suppress the regulatory function of the β-subunit in VDCC inactivation.

In PC12 cells, biphasic voltage dependence of inactivation was observed for native VDCC currents (Fig. 7*C*, *bottom*). In the recombinant expression system, a similar biphasic inactivation curve was observed in the presence of BADN, suggesting that a dominant negative effect of BADN partially dissociates the RIMs from the VDCC complexes. Furthermore, $V_{0.5}$ values of the low voltage-induced phase and the high voltage-induced phase were similar to those of inactivation curves without RIMs and with RIMs, respectively, whereas the proportions of each phase were affected by RIMs (Fig. 2 and supplemental Table S2). These findings suggest that at least two types of VDCC complexes, one with RIMs and the other without RIMs, coexist in PC12 cells. VDCC complexes not associated with RIMs may be weakly and indirectly linked to neurotransmitter release in PC12 cells, because knockdown of all four RIMs markedly decreased but did not completely abolish Ca^{2+} influx-triggered neurotransmitter release (Fig. 9).

When voltage-dependent inactivation of VDCCs is suppressed by RIMs, the responses to depolarizing membrane potentials of Ca^{2+} sensors, such as synaptotagmins, can be potentiated at presynaptic active zones. RIM-VDCC association can thus support synaptic plasticity by regulating depolarization-dependent neurotransmitter release. In PC12 cells, expression of both α-RIMs and γ-RIMs enhanced depolarization-dependent neurotransmitter release (Fig. 9*A*). Thus, not only α-RIMs but also γ-RIMs may play an important role in Ca^{2+} influx-triggered exocytosis in neuroendocrine cells, such as PC12 cells. In the case of α-RIMs, such as RIM1α, their association with VDCC β-subunits supports release via two distinct mechanisms: sustaining Ca^{2+} influx, as described above, and anchoring neurotransmitter-containing vesicles in the vicinity of VDCCs (12). The former function requires only the RIM1α C terminus (RIM1α(1258–1463)), which is conserved among RIMs, whereas the latter function requires the "full-length" structure of α-RIMs. Because γ-RIMs exert only the former function, they can act as dominant negative suppressors of vesicle docking. In fact, knockdown of RIM3γ and RIM4γ by specific siRNAs increased the number of neurotransmitter vesicles anchored near the plasma membrane in PC12 cells (Fig. 8). In addition, the expression of α-RIMs enhanced neurotransmitter release more significantly than did γ-RIMs upon depolarization elicited by 51.1 mM K^+ (Fig. 9*A*), and knockdown of α-RIMs decreased neurotransmitter release more prominently than γ-RIMs upon moderate depolarization elicited by 28.4 mM K^+ in PC12 cells (Fig. 9*C*). Upon depolarization elicited by 51.1 mM K^+, neurotransmitter release in cells with knockdown of α-RIMs and in cells with knockdown of γ-RIMs was indistinguishable (Fig. 9*B*). This is presumably because the robustness of global $[Ca^{2+}]_i$ elevation upon 51.1 mM K^+ stimulation (Fig. 9, *D* and *E*) masks the vesicle-anchoring effect of α-RIMs in PC12 cells. Importantly, compared with 51.1 mM K^+, 28.4 mM K^+ induced global $[Ca^{2+}]_i$ elevation by an order of magnitude less (Fig. 9, *D* and *E*) but ACh secretion by only 50% less (Fig. 9, *B* and *C*), suggesting that 28.4 mM K^+ is a depolarizing stimulation almost sufficient for physiological ACh secretion in PC12 cells. Hence, the presence of two functionally different groups of RIMs, α-RIMs and γ-RIMs, becomes physiologically relevant only at moderate stimulations and $[Ca^{2+}]_i$ elevations in ACh secretion from PC12 cells. By contrast, in cerebellar neurons, contributions of α-RIMs and γ-RIMs to glutamate secretion were differentiated even upon robust depolarization elicited by 51.1 mM K^+ stimulation (Fig. 10*B*). We can therefore hypothesize that a transition of the associating partner of presynaptic VDCCs between α-RIMs and γ-RIMs would modify the tightness of coupling of Ca^{2+} influx with fusion of synaptic vesicles and eventually modulate the efficacy of synaptic transmission.

Relative contributions of α-RIMs and γ-RIMs in neurotransmitter release are very likely different between neurons and PC12 cells. In particular, glutamate release is less reduced by knockdown of all RIMs (shRIM1&2&3&4) than by knockdown of α-RIMs (shRIM1&2) in cerebellar neurons in contrast to ACh release in PC12 cells (Fig. 10*B*), suggesting that contributions to neurotransmitter release of γ-RIMs through "inhibition" of vesicle anchoring to VDCCs is greater in cerebellar neurons than in neuroendocrine PC12 cells. This is presumably because knockdown of all RIMs abolishes the inhibition of anchoring by γ-RIMs and, at the same time, the enhancement of anchoring by α-RIMs, whereas knockdown of only α-RIMs

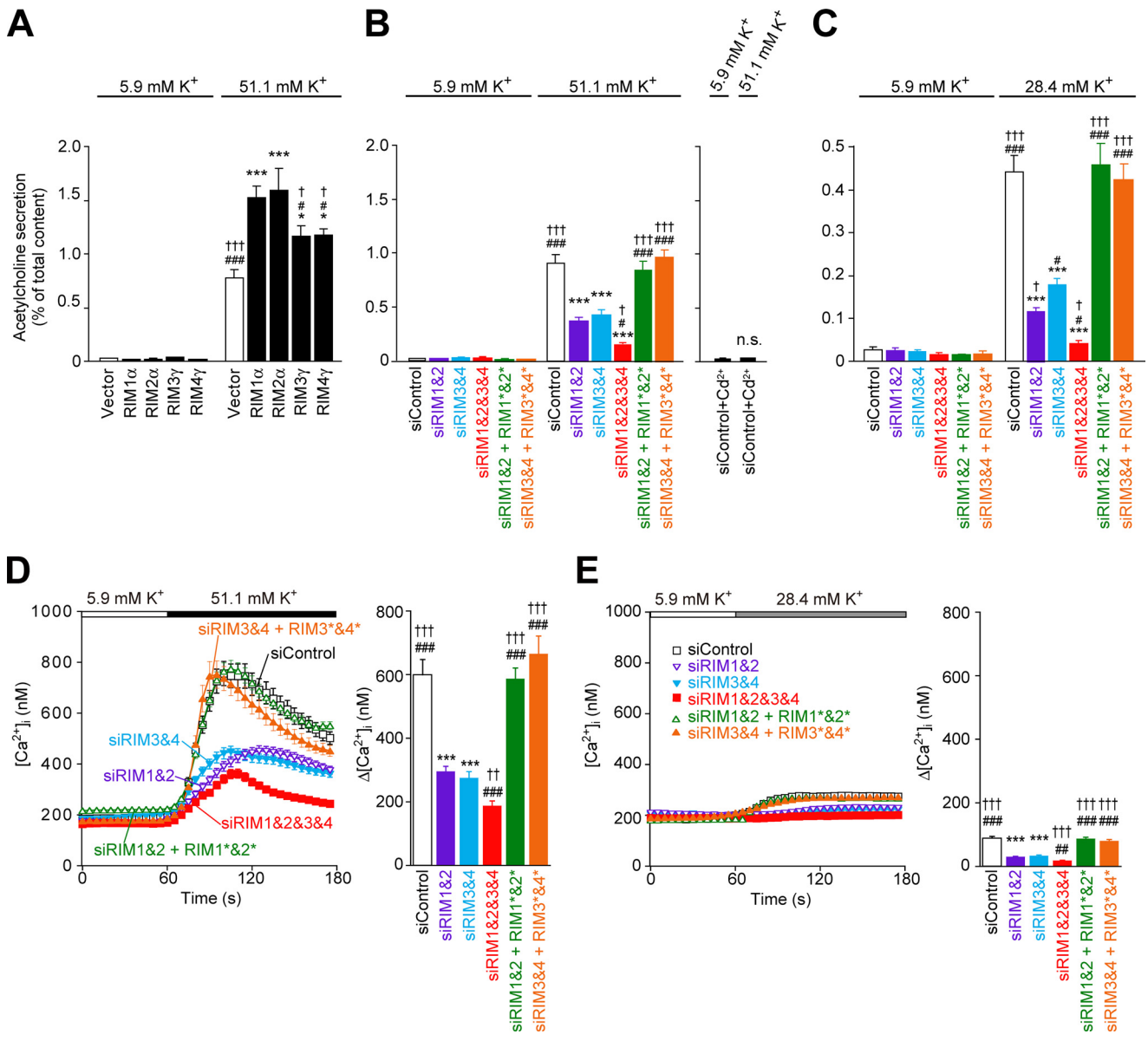

FIGURE 9. **γ-RIMs enhance neurotransmitter release less potently than α-RIMs in PC12 cells.** *A*, effects of recombinant RIMs on depolarization-dependent release of ACh from ChAT-cotransfected PC12 cells. Transfected PC12 cells are incubated for 30 s with 5.9 mM K^+ solution at 37 °C. The release of ACh during this period is considered to be basal release. To measure depolarization-induced ACh release, the cells are then incubated for 30 s with 51.1 mM K^+ solution. The amount of secreted ACh was determined as a percentage of the cellular content for each dish. The numbers of experiments performed were 12, 10, 11, 10, and 12 for transfection of vector, RIM1α, RIM2α, RIM3γ, and RIM4γ, respectively. *, $p < 0.05$; ***, $p < 0.001$ *versus* vector. #, $p < 0.05$; ###, $p < 0.001$ *versus* RIM1α. †, $p < 0.05$; †††, $p < 0.001$ *versus* RIM2α. *B* (*left*), effects of siRNA for RIMs on depolarization-dependent release of ACh from ChAT-cotransfected PC12 cells. The numbers of experiments performed were 12, 12, 11, 6, 9, and 11 for transfection of siControl, siRIM1&2, siRIM3&4, siRIM1&2&3&4, siRIM1&2 + RIM1*&2*, and siRIM3&4 + RIM3*&4*, respectively. ***, $p < 0.001$ *versus* siControl. #, $p < 0.05$; ###, $p < 0.001$ *versus* siRIM1&2. †, $p < 0.05$; †††, $p < 0.001$ *versus* siRIM3&4. *Right*, effects of 0.3 mM Cd^{2+} on depolarization-dependent release of ACh from ChAT-cotransfected PC12 cells. The number of experiments performed was 4. *n.s.*, not significant. *C*, effects of siRNA for RIMs on moderate depolarization-dependent release of ACh from ChAT-cotransfected PC12 cells. To measure ACh release, the cells were incubated for 120 s with a 28.4 mM K^+ solution. The numbers of experiments performed were 9, 10, 11, 7, 7, and 11 for transfection of siControl, siRIM1&2, siRIM3&4, siRIM1&2&3&4, siRIM1&2 + RIM1*&2*, and siRIM3&4 + RIM3*&4*, respectively. ***, $p < 0.001$ *versus* siControl. #, $p < 0.05$; ###, $p < 0.001$ *versus* siRIM1&2. †, $p < 0.05$; †††, $p < 0.001$ *versus* siRIM3&4. *D*, effects of siRIMs on Ca^{2+} responses upon elevation of extracellular K^+ concentration from 5.9 to 51.1 mM. Average time courses (*left*) and maximal $[Ca^{2+}]_i$ rises (*right*) are shown. Numbers of PC12 cells analyzed were 46, 85, 90, 72, 45, and 49 for transfection of siControl, siRIM1&2, siRIM3&4, siRIM1&2&3&4, siRIM1&2 + RIM1*&2*, and siRIM3&4 + RIM3*&4*, respectively. ***, $p < 0.001$ *versus* siControl. ###, $p < 0.001$ *versus* siRIM1&2. ††, $p < 0.01$; †††, $p < 0.001$ *versus* siRIM3&4. *E*, effects of siRIMs on Ca^{2+} responses upon elevation of extracellular K^+ concentration from 5.9 to 28.4 mM. Numbers of PC12 cells analyzed were 80, 92, 90, 97, 49, and 66 for transfection of siControl, siRIM1&2, siRIM3&4, siRIM1&2&3&4, siRIM1&2 + RIM1*&2*, and siRIM3&4 + RIM3*&4*, respectively. ***, $p < 0.001$ *versus* siControl. ##, $p < 0.01$; ###, $p < 0.001$ *versus* siRIM1&2. †††, $p < 0.001$ *versus* siRIM3&4. *Error bars*, S.E.

allows an effective inhibition of anchoring by γ-RIMs left intact in neurons. In support of this idea, it has been previously demonstrated that Ca^{2+}-triggered release is decreased ~10-fold in neurons from mice deficient in both α-RIMs (48). Furthermore, the prestimulus docking is thought to facilitate fusion and be a preparatory step for exocytosis in neurons (10). On the other hand, in PC12 cells, which possess small vesicles in addition to large dense core vesicles, there is little prestimulus docking for ACh-containing small vesicles (73). It should also be considered that knockdown efficiency is slightly reduced in

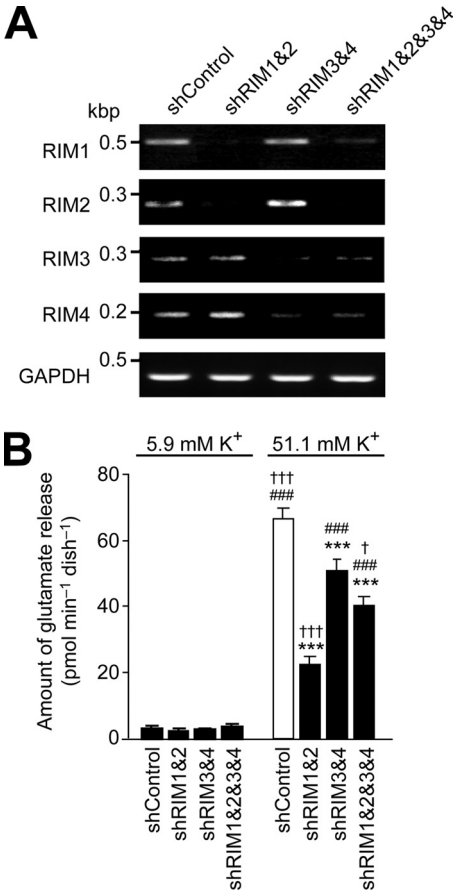

FIGURE 10. **γ-RIMs support neurotransmitter release in cerebellar neurons.** *A*, RT-PCR analysis of RNA expression of RIMs in cultured cerebellar neurons treated with a negative control shRNA vector (*shControl*), combination of RIM1- and RIM2-targeted shRNA vectors (*shRIM1&2*), combination of RIM3- and RIM4-targeted shRNA vectors (*shRIM3&4*), and combination of RIM1-, RIM2-, RIM3-, and RIM4-targeted shRNA vectors (*shRIM1&2&3&4*). GAPDH was used as an internal control. PCR was performed 26 cycles for RIM1, 30 cycles for RIM2, 36 cycles for RIM3, 36 cycles for RIM4, 30 cycles for GAPDH. *B*, effects of shRNA for RIMs on depolarization-dependent release of glutamate from cultured cerebellar neurons. Cultured cerebellar neurons transfected with shRNA vectors (10 DIV) were incubated for 1 min with the low K^+ solution (5.9 mM K^+) at 37 °C. The release of glutamate during this period was considered to be basal release. To measure glutamate release, the cells were then incubated for 1 min with a high K^+ solution (51.1 mM K^+). Numbers of experiments performed were 11, 11, 16, and 11 for transfection of shControl, shRIM1&2, shRIM3&4, and shRIM1&2&3&4, respectively. ***, $p <$ 0.001 *versus* shControl. ###, $p < 0.001$ *versus* shRIM1&2. †, $p < 0.05$; †††, $p <$ 0.001 *versus* shRIM3&4. *Error bars*, S.E.

shRIM1&2&3&4, as demonstrated by residual expression of RIM1 and RIM3 in Fig. 10*A*. The transfection efficiency of each plasmid can be reduced when four shRNA vectors are simultaneously transfected.

In central neurons, overlapping distributions of RIM isoforms revealed by *in situ* hybridization (Fig. 5) (35, 48) suggested that RIM isoforms coexist in the same neurons in the brain. Redundant functions of RIM1α and RIM2α in Ca^{2+}-triggered neurotransmitter release have been reported, but α-RIMs were not replaceable by γ-RIMs with regard to their role in neurotransmitter release (48). This supports the possibility that α-RIMs and γ-RIMs function antagonistically in terms of vesicle anchoring to VDCCs and may also suggest that γ-RIMs are involved in physiological functions other than neurotransmitter release in neurons. Different subcellular distributions of RIMs support this hypothesis; whereas RIM1α is a presynaptic protein (32, 39), RIM3γ is present in many neuronal dendrites and dendritic spines, especially in or near the postsynaptic densities (35). Interestingly, studies on the subcellular localization of the P/Q- and R-type channels have defined both axonal and somatodendritic localizations in contrast to the constrained nerve terminal localization of N-type channels (74–76). Thus, in regulation of VDCC inactivation, the respective RIM isoforms may interact with particular VDCC types at axonal and somatodendritic regions and at presynaptic regions in neurons.

In terms of $Ca_V2.1$, which forms P/Q-type VDCCs, the P-type current characterized by very slow inactivation kinetics was first identified in cerebellar Purkinje cells (77, 78), whereas the Q-type current characterized by fast inactivation kinetics was later identified in cerebellar granule cells (79, 80). Although P- and Q-type VDCCs show distinct properties, knock-out studies have clearly demonstrated that both are encoded by the same $Ca_V2.1$ gene (80, 81). In addition, recombinant human $Ca_V2.1$ expressed in HEK cells produced the Q-type current but failed to produce the P-type current (82). However, the P-type current was recorded in knock-in mice that express the human $Ca_V2.1$ instead of mouse $Ca_V2.1$ (83). These results suggest that some additional factors, such as post-translational modification or interaction with other proteins, may be necessary to produce the P-type current. An interesting candidate that determines the channel types of the $Ca_V2.1$-forming channel is RIMs. This idea is supported by the following findings. First, our *in situ* hybridization of cerebellar sections revealed that RIM3γ and RIM4γ are more highly expressed in Purkinje cells than in granule cells (Fig. 5, *A* (*e*) and *B* (*e*)). Second, RIM3γ has been reported as a postsynaptic protein in the molecular layer of the cerebellar cortex, which contains dendrites of Purkinje cells (35), and P-type has also been located in the dendrites and soma of Purkinje cells (77, 84).

In conclusion, we present a common physiological function for RIM proteins, maintaining Ca^{2+} influx triggered by depolarization through suppression of VDCC inactivation. As observed in PC12 cells and cerebellar neurons, specific physiological roles played by γ-RIMs can weaken the physical coupling of VDCCs with synaptic vesicles. Further studies using γ-RIM knock-out mice are necessary to test this hypothesis and reveal its relevance to neural processes.

Acknowledgments—We greatly appreciate the gifts of NPY-Venus from A. Miyawaki and pEFmChAT from M. Takahashi, and we thank K. Yamazaki and N. Yokoi for expert experiments.

REFERENCES

1. Sheng, M., and Hoogenraad, C. C. (2007) *Annu. Rev. Biochem.* **76,** 823–847
2. Ohtsuka, T., Takao-Rikitsu, E., Inoue, E., Inoue, M., Takeuchi, M., Matsubara, K., Deguchi-Tawarada, M., Satoh, K., Morimoto, K., Nakanishi, H., and Takai, Y. (2002) *J. Cell Biol.* **158,** 577–590
3. Zhai, R. G., and Bellen, H. J. (2004) *Physiology* **19,** 262–270
4. Sudhof, T. C. (2004) *Annu. Rev. Neurosci.* **27,** 509–547
5. Schoch, S., and Gundelfinger, E. D. (2006) *Cell Tissue Res.* **326,** 379–391
6. Wojcik, S. M., and Brose, N. (2007) *Neuron* **55,** 11–24
7. Stanley, E. F. (1993) *Neuron* **11,** 1007–1011

8. Sheng, Z. H., Rettig, J., Takahashi, M., and Catterall, W. A. (1994) *Neuron* **13,** 1303–1313
9. Bezprozvanny, I., Scheller, R. H., and Tsien, R. W. (1995) *Nature* **378,** 623–626
10. Neher, E. (1998) *Neuron* **20,** 389–399
11. Wadel, K., Neher, E., and Sakaba, T. (2007) *Neuron* **53,** 563–575
12. Kiyonaka, S., Wakamori, M., Miki, T., Uriu, Y., Nonaka, M., Bito, H., Beedle, A. M., Mori, E., Hara, Y., De Waard, M., Kanagawa, M., Itakura, M., Takahashi, M., Campbell, K. P., and Mori, Y. (2007) *Nat. Neurosci.* **10,** 691–701
13. Catterall, W. A., and Few, A. P. (2008) *Neuron* **59,** 882–901
14. Tsien, R. W., Ellinor, P. T., and Horne, W. A. (1991) *Trends Pharmacol. Sci.* **12,** 349–354
15. Takahashi, T., and Momiyama, A. (1993) *Nature* **366,** 156–158
16. Wheeler, D. B., Randall, A., and Tsien, R. W. (1994) *Science* **264,** 107–111
17. Catterall, W. A. (1998) *Cell Calcium* **24,** 307–323
18. Ertel, E. A., Campbell, K. P., Harpold, M. M., Hofmann, F., Mori, Y., Perez-Reyes, E., Schwartz, A., Snutch, T. P., Tanabe, T., Birnbaumer, L., Tsien, R. W., and Catterall, W. A. (2000) *Neuron* **25,** 533–535
19. Zhong, H., Yokoyama, C. T., Scheuer, T., and Catterall, W. A. (1999) *Nat. Neurosci.* **2,** 939–941
20. Maximov, A., Südhof, T. C., and Bezprozvanny, I. (1999) *J. Biol. Chem.* **274,** 24453–24456
21. Maximov, A., and Bezprozvanny, I. (2002) *J. Neurosci.* **22,** 6939–6952
22. Spafford, J. D., and Zamponi, G. W. (2003) *Curr. Opin. Neurobiol.* **13,** 308–314
23. Nishimune, H., Sanes, J. R., and Carlson, S. S. (2004) *Nature* **432,** 580–587
24. Kang, M. G., Chen, C. C., Wakamori, M., Hara, Y., Mori, Y., and Campbell, K. P. (2006) *Proc. Natl. Acad. Sci. U.S.A.* **103,** 5561–5566
25. Mori, Y., Friedrich, T., Kim, M. S., Mikami, A., Nakai, J., Ruth, P., Bosse, E., Hofmann, F., Flockerzi, V., Furuichi, T., Mikoshiba, K., Imoto, K., Tanabe, T., and Numa, S. (1991) *Nature* **350,** 398–402
26. Bichet, D., Cornet, V., Geib, S., Carlier, E., Volsen, S., Hoshi, T., Mori, Y., and De Waard, M. (2000) *Neuron* **25,** 177–190
27. Varadi, G., Lory, P., Schultz, D., Varadi, M., and Schwartz, A. (1991) *Nature* **352,** 159–162
28. Lacerda, A. E., Kim, H. S., Ruth, P., Perez-Reyes, E., Flockerzi, V., Hofmann, F., Birnbaumer, L., and Brown, A. M. (1991) *Nature* **352,** 527–530
29. Béguin, P., Nagashima, K., Gonoi, T., Shibasaki, T., Takahashi, K., Kashima, Y., Ozaki, N., Geering, K., Iwanaga, T., and Seino, S. (2001) *Nature* **411,** 701–706
30. Hibino, H., Pironkova, R., Onwumere, O., Rousset, M., Charnet, P., Hudspeth, A. J., and Lesage, F. (2003) *Proc. Natl. Acad. Sci. U.S.A.* **100,** 307–312
31. Vendel, A. C., Terry, M. D., Striegel, A. R., Iverson, N. M., Leuranguer, V., Rithner, C. D., Lyons, B. A., Pickard, G. E., Tobet, S. A., and Horne, W. A. (2006) *J. Neurosci.* **26,** 2635–2644
32. Wang, Y., Okamoto, M., Schmitz, F., Hofmann, K., and Südhof, T. C. (1997) *Nature* **388,** 593–598
33. Wang, Y., and Südhof, T. C. (2003) *Genomics* **81,** 126–137
34. Kaeser, P. S., Kwon, H. B., Chiu, C. Q., Deng, L., Castillo, P. E., and Südhof, T. C. (2008) *J. Neurosci.* **28,** 13435–13447
35. Liang, F., Zhang, B., Tang, J., Guo, J., Li, W., Ling, E. A., Chu, H., Wu, Y., Chan, Y. G., and Cao, Q. (2007) *J. Comp. Neurol.* **503,** 501–510
36. Wang, Y., Sugita, S., and Sudhof, T. C. (2000) *J. Biol. Chem.* **275,** 20033–20044
37. Betz, A., Thakur, P., Junge, H. J., Ashery, U., Rhee, J. S., Scheuss, V., Rosenmund, C., Rettig, J., and Brose, N. (2001) *Neuron* **30,** 183–196
38. Coppola, T., Magnin-Luthi, S., Perret-Menoud, V., Gattesco, S., Schiavo, G., and Regazzi, R. (2001) *J. Biol. Chem.* **276,** 32756–32762
39. Schoch, S., Castillo, P. E., Jo, T., Mukherjee, K., Geppert, M., Wang, Y., Schmitz, F., Malenka, R. C., and Südhof, T. C. (2002) *Nature* **415,** 321–326
40. Stanley, E. F., and Goping, G. (1991) *J. Neurosci.* **11,** 985–993
41. Forsythe, I. D., Tsujimoto, T., Barnes-Davies, M., Cuttle, M. F., and Takahashi, T. (1998) *Neuron* **20,** 797–807
42. Johnson, S., Halford, S., Morris, A. G., Patel, R. J., Wilkie, S. E., Hardcastle, A. J., Moore, A. T., Zhang, K., and Hunt, D. M. (2003) *Genomics* **81,** 304–314
43. Miki, T., Kiyonaka, S., Uriu, Y., De Waard, M., Wakamori, M., Beedle, A. M., Campbell, K. P., and Mori, Y. (2007) *Channels* **1,** 144–147
44. Castillo, P. E., Schoch, S., Schmitz, F., Südhof, T. C., and Malenka, R. C. (2002) *Nature* **415,** 327–330
45. Fourcaudot, E., Gambino, F., Humeau, Y., Casassus, G., Shaban, H., Poulain, B., and Lüthi, A. (2008) *Proc. Natl. Acad. Sci. U.S.A.* **105,** 15130–15135
46. Lachamp, P. M., Liu, Y., and Liu, S. J. (2009) *J. Neurosci.* **29,** 381–392
47. Calakos, N., Schoch, S., Südhof, T. C., and Malenka, R. C. (2004) *Neuron* **42,** 889–896
48. Schoch, S., Mittelstaedt, T., Kaeser, P. S., Padgett, D., Feldmann, N., Chevaleyre, V., Castillo, P. E., Hammer, R. E., Han, W., Schmitz, F., Lin, W., and Südhof, T. C. (2006) *EMBO J.* **25,** 5852–5863
49. Weimer, R. M., Gracheva, E. O., Meyrignac, O., Miller, K. G., Richmond, J. E., and Bessereau, J. L. (2006) *J. Neurosci.* **26,** 8040–8047
50. Gracheva, E. O., Hadwiger, G., Nonet, M. L., and Richmond, J. E. (2008) *Neurosci. Lett.* **444,** 137–142
51. Ozaki, N., Shibasaki, T., Kashima, Y., Miki, T., Takahashi, K., Ueno, H., Sunaga, Y., Yano, H., Matsuura, Y., Iwanaga, T., Takai, Y., and Seino, S. (2000) *Nat. Cell Biol.* **2,** 805–811
52. Wong, F. K., and Stanley, E. F. (2010) *J. Neurochem.* **112,** 463–473
53. Niidome, T., Teramoto, T., Murata, Y., Tanaka, I., Seto, T., Sawada, K., Mori, Y., and Katayama, K. (1994) *Biochem. Biophys. Res. Commun.* **203,** 1821–1827
54. Wakamori, M., Yamazaki, K., Matsunodaira, H., Teramoto, T., Tanaka, I., Niidome, T., Sawada, K., Nishizawa, Y., Sekiguchi, N., Mori, E., Mori, Y., and Imoto, K. (1998) *J. Biol. Chem.* **273,** 34857–34867
55. Zhu, L. J., and Altmann, S. W. (2005) *Anal. Biochem.* **345,** 102–109
56. Kagawa, T., Ikenaka, K., Inoue, Y., Kuriyama, S., Tsujii, T., Nakao, J., Nakajima, K., Aruga, J., Okano, H., and Mikoshiba, K. (1994) *Neuron* **13,** 427–442
57. Itakura, M., Misawa, H., Sekiguchi, M., Takahashi, S., and Takahashi, M. (1999) *Biochem. Biophys. Res. Commun.* **265,** 691–696
58. Tsuboi, T., and Fukuda, M. (2006) *J. Cell Sci.* **119,** 2196–2203
59. Nishida, M., Nagao, T., and Kurose, H. (1999) *Biochem. Biophys. Res. Commun.* **262,** 350–354
60. Patzel, V., Rutz, S., Dietrich, I., Köberle, C., Scheffold, A., and Kaufmann, S. H. E. (2005) *Nat. Biotechnol.* **23,** 1440–1444
61. Koga, T., Kozaki, S., and Takahashi, M. (2002) *Brain Res.* **952,** 282–289
62. Castellano, A., Wei, X., Birnbaumer, L., and Perez-Reyes, E. (1993) *J. Biol. Chem.* **268,** 3450–3455
63. Castellano, A., Wei, X., Birnbaumer, L., and Perez-Reyes, E. (1993) *J. Biol. Chem.* **268,** 12359–12366
64. Ruth, P., Röhrkasten, A., Biel, M., Bosse, E., Regulla, S., Meyer, H. E., Flockerzi, V., and Hofmann, F. (1989) *Science* **245,** 1115–1118
65. Hullin, R., Singer-Lahat, D., Freichel, M., Biel, M., Dascal, N., Hofmann, F., and Flockerzi, V. (1992) *EMBO J.* **11,** 885–890
66. Plummer, M. R., Logothetis, D. E., and Hess, P. (1989) *Neuron* **2,** 1453–1463
67. Liu, H., Felix, R., Gurnett, C. A., De Waard, M., Witcher, D. R., and Campbell, K. P. (1996) *J. Neurosci.* **16,** 7557–7565
68. Gebhart, M., Juhasz-Vedres, G., Zuccotti, A., Brandt, N., Engel, J., Trockenbacher, A., Kaur, G., Obermair, G. J., Knipper, M., Koschak, A., and Striessnig, J. (2010) *Mol. Cell Neurosci.* **44,** 246–259
69. Shibasaki, T., Sunaga, Y., Fujimoto, K., Kashima, Y., and Seino, S. (2004) *J. Biol. Chem.* **279,** 7956–7961
70. Hibino, H., Pironkova, R., Onwumere, O., Vologodskaia, M., Hudspeth, A. J., and Lesage, F. (2002) *Neuron* **34,** 411–423
71. De Waard, M., Pragnell, M., and Campbell, K. P. (1994) *Neuron* **13,** 495–503
72. Richards, M. W., Leroy, J., Pratt, W. S., and Dolphin, A. C. (2007) *Channels* **1,** 92–101
73. Liu, T. T., Kishimoto, T., Hatakeyama, H., Nemoto, T., Takahashi, N., and Kasai, H. (2005) *J. Physiol.* **568,** 917–929
74. Westenbroek, R. E., Hoskins, L., and Catterall, W. A. (1998) *J. Neurosci.* **15,** 6319–6330
75. Craig, P. J., McAinsh, A. D., McCormack, A. L., Smith, W., Beattie, R. E.,

Priestley, J. V., Yip, J. L., Averill, S., Longbottom, E. R., and Volsen, S. G. (1998) *J. Comp. Neurol.* **397,** 251–267
76. Hanson, J. E., and Smith, Y. (2002) *J. Comp. Neurol.* **442,** 89–98
77. Llinás, R., Sugimori, M., Lin, J. W., and Cherksey, B. (1989) *Proc. Natl. Acad. Sci. U.S.A.* **86,** 1689–1693
78. Randall, A., and Tsien, R. W. (1995) *J. Neurosci.* **15,** 2995–3012
79. Sather, W. A., Tanabe, T., Zhang, J. F., Mori, Y., Adams, M. E., and Tsien, R. W. (1993) *Neuron* **11,** 291–303
80. Jun, K., Piedras-Rentería, E. S., Smith, S. M., Wheeler, D. B., Lee, S. B., Lee, T. G., Chin, H., Adams, M. E., Scheller, R. H., Tsien, R. W., and Shin, H. S. (1999) *Proc. Natl. Acad. Sci. U.S.A.* **96,** 15245–15250
81. Fletcher, C. F., Tottene, A., Lennon, V. A., Wilson, S. M., Dubel, S. J., Paylor, R., Hosford, D. A., Tessarollo, L., McEnery, M. W., Pietrobon, D., Copeland, N. G., and Jenkins, N. A. (2001) *FASEB J.* **15,** 1288–1290
82. Toru, S., Murakoshi, T., Ishikawa, K., Saegusa, H., Fujigasaki, H., Uchihara, T., Nagayama, S., Osanai, M., Mizusawa, H., and Tanabe, T. (2000) *J. Biol. Chem.* **275,** 10893–10898
83. Saegusa, H., Wakamori, M., Matsuda, Y., Wang, J., Mori, Y., Zong, S., and Tanabe, T. (2007) *Mol. Cell Neurosci.* **34,** 261–270
84. Llinás, R., and Sugimori, M. (1980) *J. Physiol.* **305,** 197–213

Supplemental Data

Supplemental Experimental Procedures

Confocal imaging- PC12 cells were cotransfected with pVenus-N1-NPY or pEGFP-N1 and mixture of RIM siRNAs using OptiFect (invitrogen). Thirty-six h after transfection, PC12 cells were plated onto poly-L-lysine coated glass coverslips. Forty-eight h after transfection, cells were fixed, permeabilized, and stained with anti-RIM1/2 polyclonal antibody (Synaptic Systems 140-203) or anti-Syntaxin monoclonal antibody (Sigma S0664) and Cy3-conjugated secondary antibody (Invitrogen). Fluorescence images were acquired with a confocal laser-scanning microscope (Olympus FV500) using the 488-nm line of an argon laser for excitation and a 505-nm to 525-nm band-pass filter for emission (Venus and EGFP), or the 543-nm line of a HeNe laser for excitation and a 560-nm long-pass filter for emission (Cy3). The specimens were viewed at high magnification using plan oil objectives (× 60, 1.40 numerical aperture (NA), Olympus).

TIRF imaging of RIM1 and RIM2 immunoreactivity- pDs-Red-monomer-N1 (Clontech) and mixture of RIMs siRNAs were transfected into PC12 cells. Thirty-six h after transfection, PC12 cells were plated onto poly-L-lysine coated glass coverslips. Forty-eight h after transfection, cells were fixed, permeabilized, and stained with anti-RIM1/2 polyclonal antibody (Synaptic Systems 140-203) and Alexa Fluor-488-conjugated anti-rabbit secondary antibody (Invitrogen). TIRF images were obtained using 100 x 1.45-numerical-aperture TIRF objective fitted to an inverted microscope system (Olympus IX71) and a 488-nm laser line (kyma488, 20 milliwatt, MELLES GRIOT), and images were acquired using a cooled CCD camera (EM-CCD Hamamatsu Photonics) and recorded with Metamorph software (Molecular Devices). Area and fluorescent intensity calculations were also performed using Metamorph software. Relative intensities of RIM1/2 immunoreactivity were estimated by normalizing average intensity in Ds-Red positive cells to that in Ds-Red negative cells in the same visual field.

Coimmunoprecipitation using PC12 cell lysate- HEK293T cells were transfected with pCMV-tag2-RIMs. Forty-eight h after transfection, HEK293T cells were solubilized in NP-40 buffer, and then centrifuged at 17400 × *g* for 20 min. The supernatant was incubated with PC12 cell lysate for 6 h at 4 °C. For coimmunoprecipitation, the mixture was incubated with anti-FLAG M2 monoclonal antibody (Sigma F3165) or polyclonal antibody (Sigma F7425). The immunocomplexes were incubated with protein A-agarose beads (Santa Cruz), and the beads were washed with NP-40 buffer. Immunoprecipitated proteins were characterized by WB. Association between Rab3 and RIMs are evaluated in the presence of 0.5 mM Guanosine-5'-O-(3-thiotriphosphate) (GTPγS). Mouse anti-Munc13 monoclonal antibody (BD Transduction Laboratory 610998), mouse anti-Rab3 monoclonal antibody (BD Transduction Laboratory 610379), and chicken anti-Liprin1-α polyclonal antibody (Sigma GW21470) were used as a primary antibody.

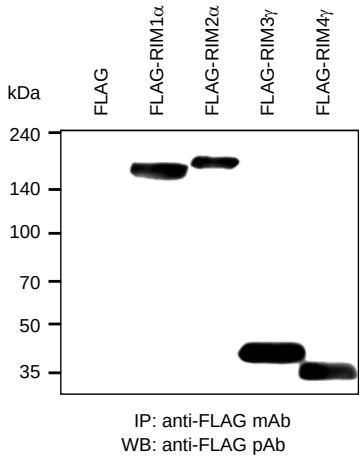

Supplemental Figure 1. Immunoprecipitation of FLAG-RIMs. FLAG-RIMs are immunoprecipitated with monoclonal anti-FLAG antibody and are analyzed by WB using polyclonal anti-FLAG antibody.

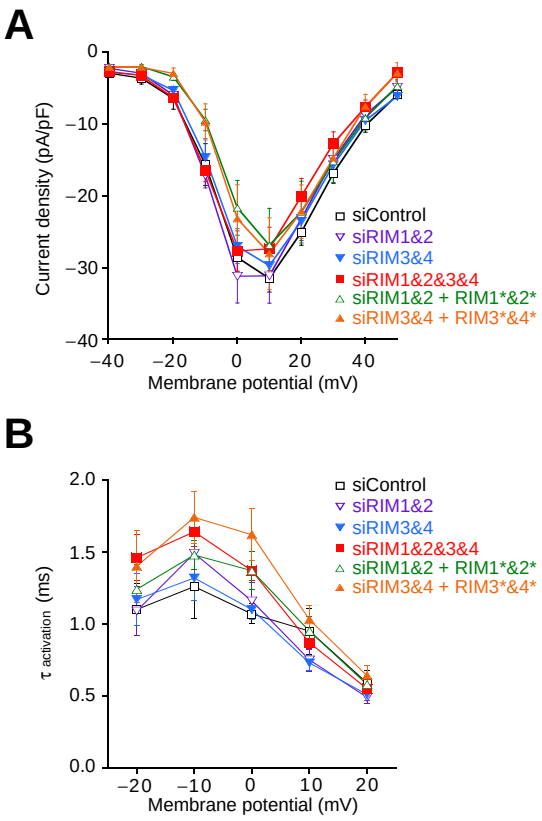

Supplemental Figure 2. Effects of siRNA for RIMs on the activation properties of VDCC currents in PC12 cells. *A*. Effects of siRNA for RIMs on *I-V* relationships in PC12 cells. Ba^{2+} currents elicited by application of 30-ms test pluses from –40 mV to 50 mV with 10-mV increments from a V_h of –80 mV are analyzed. *B*. Activation kinetics of Ba^{2+} currents in PC12 cells. Activation time constants are obtained from currents elicited by 30-ms step depolarization from –20 to 20 mV in 10-mV increments from a V_h of –80 mV and plotted as a function of test potential. See Supplemental Table S5 for statistical significance of the differences.

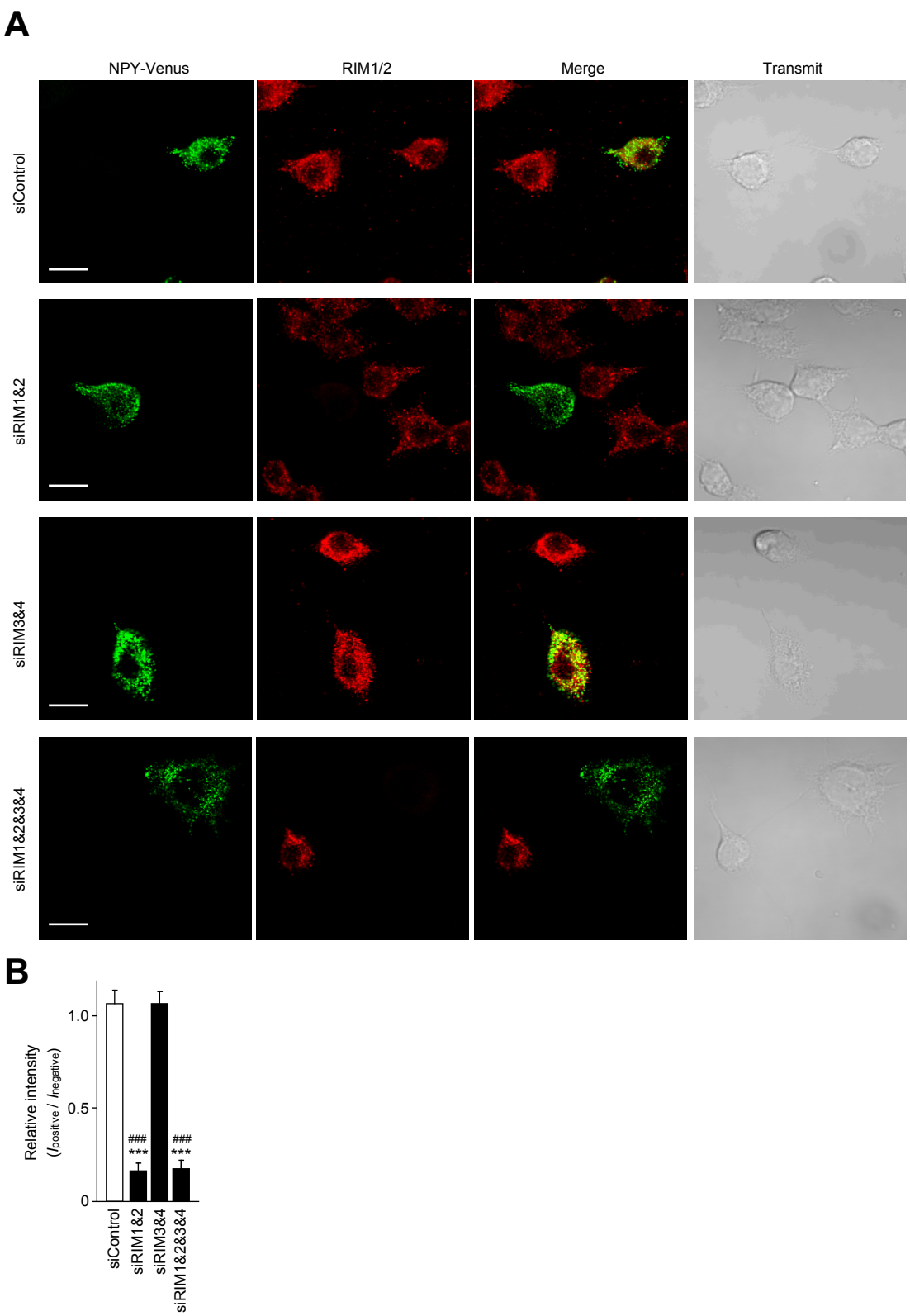

Supplemental Figure 3. Confocal images demonstrate silencing of RIM1 and RIM2 with siRNA in PC12 cells. *A*. Silencing of endogenous RIM1 and RIM2 in PC12 cells with siRNA causes reduction of RIM1 and RIM2 immunoreactivity. NPY-Venus and combination of siRNAs (siControl, siRIM1&2, siRIM3&4, or siRIM1&2&3&4) are co-transfected into PC12 cells. Forty-eight h after transfection, cells are fixed, permeabilized, and stained with anti-RIM1/2 polyclonal antibody and Cy3-conjugated anti-rabbit secondary antibody. The fluorescent image is analyzed by confocal laser microscopy. Scale bar, 10 m. *B*. Relative intensity of RIM1/2 immunoreactivity. Average intensity of RIM1/2 immunoreactivity in NPY-Venus-positive cells is normalized to that in NPY-Venus-negative cells in the same visual field. Numbers of areas observed are 14, 15, 11, and 9 for transfection of siControl, siRIM1&2, siRIM3&4, and siRIM1&2&3&4, respectively. $^{***}P < 0.001$ versus siControl. $^{\#\#\#}P < 0.001$ versus siRIM3&4.

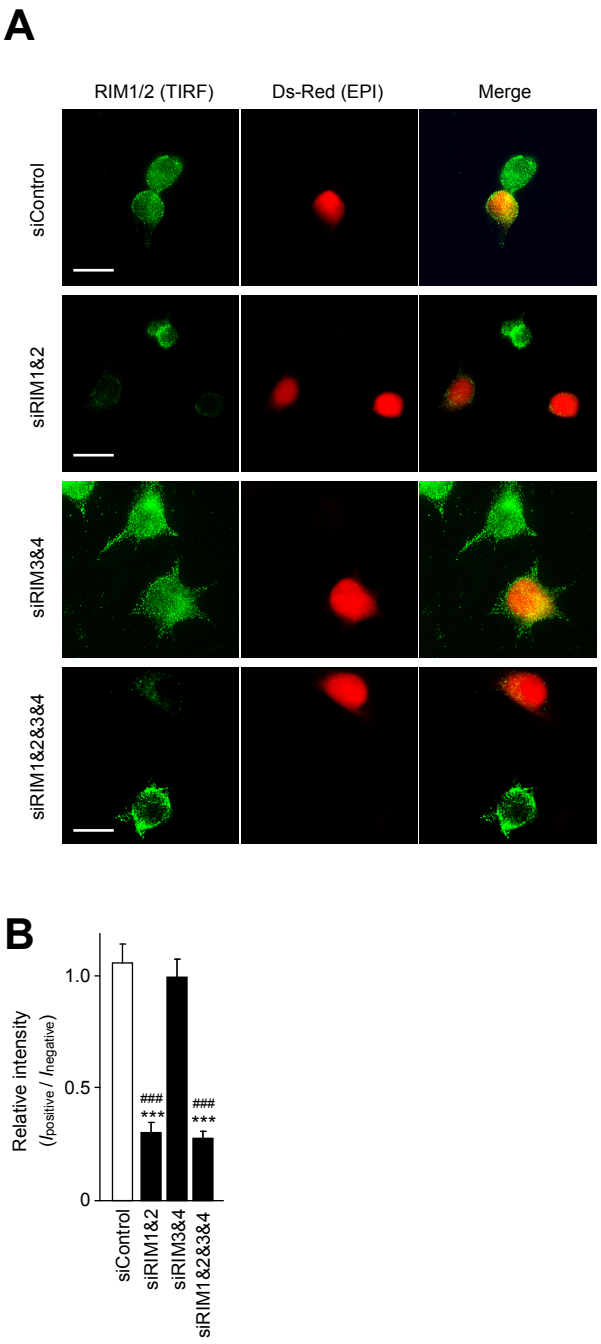

Supplemental Figure 4. TIRF images demonstrate silencing of RIM1 and RIM2 with siRNA in the plasma membrane of PC12 cells. *A*. Typical TIRF images of immunoreactivity of RIM1 and RIM2 in the plasma membrane. Ds-Red monomer and combination of siRNAs are cotransfected into PC12 cells. Forty-eight h after transfection, cells are fixed, permeabilized, and stained with anti-RIM1/2 polyclonal antibody and Alexa-Fluor-488-conjugated anti-rabbit secondary antibody. Epi-fluorescent images (EPI) are obtained for Ds-Red monomer used as a marker of transfection. Scale bar, 10 m. *B*. Relative intensity of RIM1/2 immunoreactivity. Average intensity of RIM1/2 immunoreactivity in Ds-Red-positive cells is normalized to that in Ds-Red-negative cells in the same visual field. Numbers of areas observed are 10, 18, 12, and 21 for transfection of siControl, siRIM1&2, siRIM3&4, and siRIM1&2&3&4, respectively. $^{***}P < 0.001$ versus siControl. $^{\#\#\#}P < 0.001$ versus siRIM3&4.

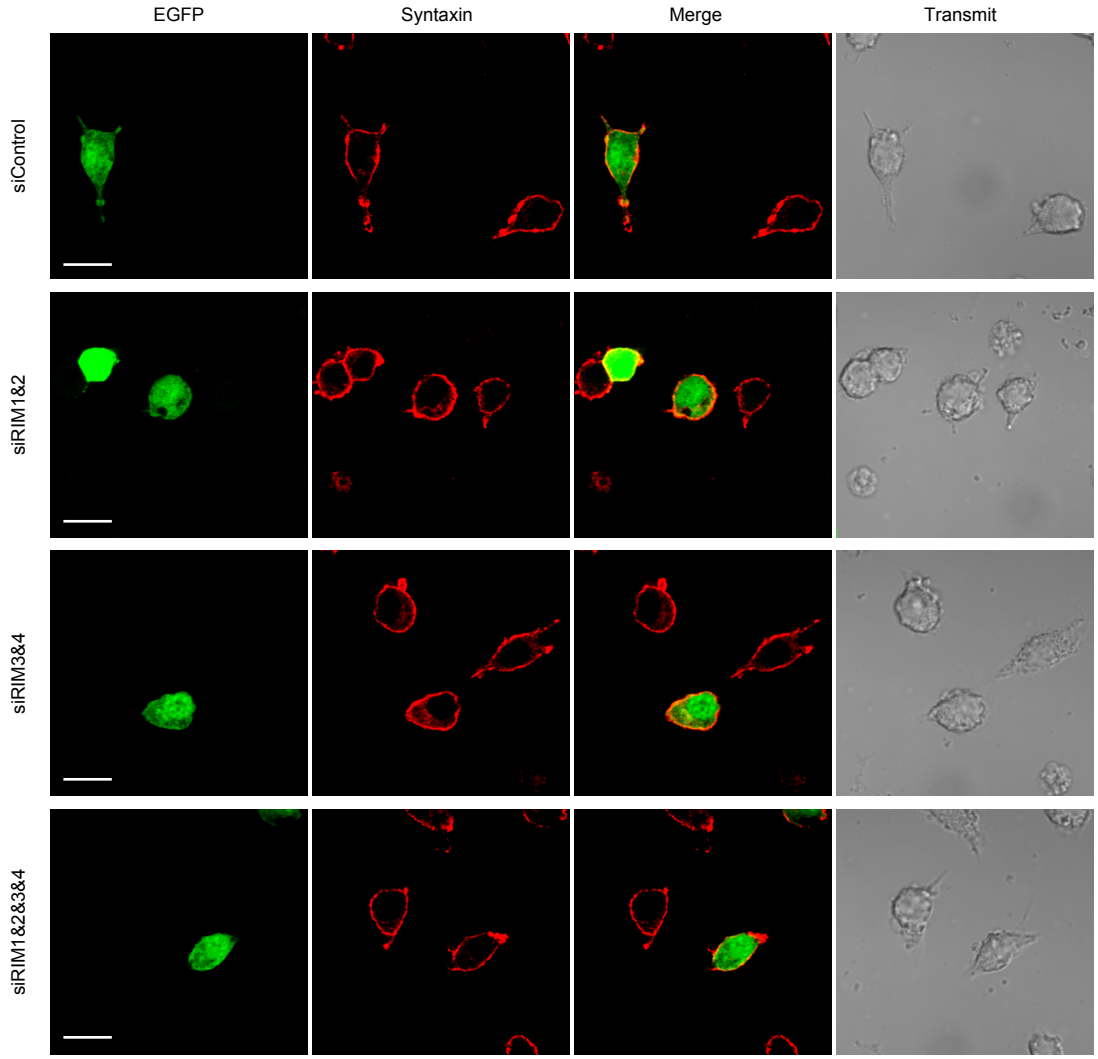

Supplemental Figure 5. Localization of syntaxin is intact in RIM knockdown PC12 cells. Silencing of endogenous RIMs in PC12 cells with siRNA fails to affect localization and intensity of syntaxin immunoreactivity. EGFP and combination of siRNAs (siControl, siRIM1&2, siRIM3&4, or siRIM1&2&3&4) are cotransfected into PC12 cells. Forty-eight h after transfection, cells are fixed, permeabilized, and stained with anti-syntaxin monoclonal antibody and Cy3-conjugated anti-mouse secondary antibody. The fluorescent image is analyzed by confocal laser microscopy. Scale bar, 10 m.

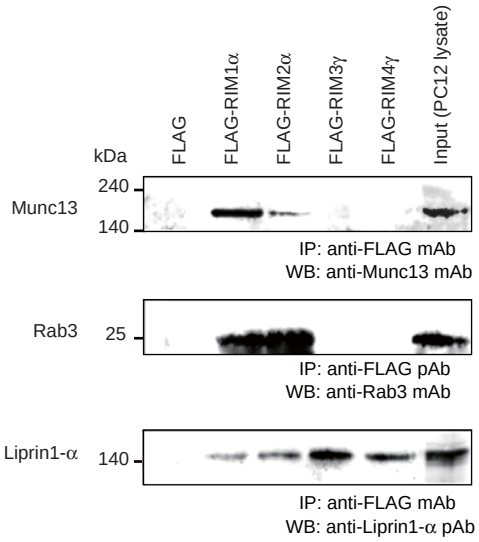

Supplemental Figure 6. Characterization of binding of synaptic proteins to RIMs. Cell lysate from HEK293T expressing FLAG-RIMs is incubated with PC12 cell lysate. FLAG-RIMs are immunoprecipitated with anti-FLAG monoclonal or polyclonal antibody and are analyzed by WB using indicated antibody. Associations between Rab3 and RIMs are evaluated in the presence of GTPγS.

SUPPLEMENTAL TABLES

Table S1 Antisense and sense PCR primers used in real-time PCR or RT-PCR analysis.

Species	Gene	Orientation	Pair of primers for PCR (5' to 3')
Mouse (for real-time PCR)	RIM1	Sense	GTTGGAGGTTGAGGTTATCAGAGCCCGGAG
		Antisense	GACGAACTTTCCAGTGATGATTGGGAAGC
	RIM2	Sense	GACAGCTGGAGGTAGAAATCATCCG
		Antisense	GAACCATCCAATCACCATGTTGGATAG
	RIM3	Sense	GTACCAGCAAGCTCTGCTCTTTGATG
		Antisense	GCCGGTGACTGCAGCACTCAGGTCCAGCTCG
	RIM4	Sense	GCTCGAAGACACTGCCAGCTGCCTATATCAAG
		Antisense	AGGACTCGAGCCACGCCCATGAACTG
	18S ribosomal RNA	Sense	GAGGTAGTGACGAAAAATAACAAT
		Antisense	TTGCCCTCCAATGGATCCT
		Antisense (Reverse Transcript)	GAGCTGGAATTACCGCGGCT
Rat (for RT-PCR)	RIM1	Sense	CAGCATCAACAGTTATAGCTCGG
		Antisense	CATCCAATCACCATGCTGGATAG
	RIM2	Sense	GGATCACAAATCCTTTATGGGAGTGG
		Antisense	CACAGGATGGCTCTTTATCCCTAGAC
	RIM3	Sense	GGATCACAAGTGCTTCATGGGTATGG
		Antisense	GGGTAAGGGGTCCAGAAGGTCATGGAG
	RIM4	Sense	GGAAACTACGGACGAATGGAGCGGAAG
		Antisense	GGGCCCCACGGTGCTCTCGAGGGACAGCTG
	β-actin	Sense	TTCTACAATGAGCTGCGTGTGGC
		Antisense	CTCATAGCTCTTCTCCAGGGAGGA
	GAPDH	Sense	ATCACCATCTTCCAGGAGCGAG
		Antisense	CAACGGATACATTGGGGGTAGG

Table S2 Effect of RIMs or BADN on inactivation properties of P/Q-type VDCC in BHK cells expressing $Ca_v2.1$, α_2/δ and β_{1b} [1) 2) 3)].

	Inactivation parameters						
	a	$V_{0.5}^{Low}$ (mV)	K^{Low} (mV)	*b*	$V_{0.5}^{High}$ (mV)	K^{High} (mV)	1–*a*–*b*
Vector	1.00 ± 0.00 (12)	−58.8 ± 2.5 (12)	−7.1 ± 0.2 (12)	0.00 ± 0.00 (12)			0.00 ± 0.00 (12)
RIM1α	0.00 ± 0.00 (6) ***			0.73 ± 0.04 (6)***	−23.4 ± 0.9 (6)	−7.8 ± 1.3 (6)	0.27 ± 0.04 (6)***
RIM1α + BADN	0.67 ± 0.06 (4) ***###	−63.6 ± 2.9 (4)	−6.2 ± 1.0 (4)	0.29 ± 0.04 (4)***###	−26.7 ± 3.7 (4)	−6.4 ± 2.4 (4)	0.04 ± 0.03 (4) #
RIM2α	0.00 ± 0.00 (6) ***			0.75 ± 0.08 (6)***	−25.8 ± 1.8 (6)	−7.4 ± 1.5 (6)	0.25 ± 0.08 (6)***
RIM2α + BADN	0.52 ± 0.11 (6) ***###	−66.6 ± 2.0 (6)	−7.3 ± 0.3 (6)	0.45 ± 0.10 (6)***#	−26.8 ± 2.8 (6)	−3.4 ± 0.4 (6)	0.04 ± 0.02 (6) #
RIM3γ	0.00 ± 0.00 (5) ***			0.81 ± 0.02 (5)***	−27.6 ± 1.6 (5)	−7.7 ± 1.2 (5)	0.19 ± 0.02 (5)***
RIM3γ + BADN	0.44 ± 0.17 (5) ***###	−72.0 ± 2.5 (5)	−5.2 ± 0.7 (5)	0.49 ± 0.14 (5)***#	−19.3 ± 6.2 (5)	−1.0 ± 2.7 (5)	0.07 ± 0.03 (5) #
RIM4γ	0.00 ± 0.00 (6) ***			0.81 ± 0.04 (6)***	−25.0 ± 1.7 (6)	−6.2 ± 1.7 (6)	0.19 ± 0.04 (6)***
RIM4γ + BADN	0.46 ± 0.15 (5) ***###	−68.9 ± 1.7 (5)	−6.8 ± 0.5 (5)	0.49 ± 0.13 (5)***#	−27.0 ± 3.2 (5)	−4.6 ± 1.2 (5)	0.04 ± 0.02 (5) ***#

1) ***$P < 0.001$ versus vector.

2) #$P < 0.05$, ###$P < 0.001$ versus without BADN.

3) Numbers of cells analyzed are indicated in the parenthesis.

Table S3 Effects of RIMs on current density and activation of P/Q-type VDCC in BHK cells expressing $Ca_v2.1$, α_2/δ and β_{1b}[1) 2)].

	Current density (pA / pF)[3)]	Activation parameters			
		$V_{0.5}$ (mV)	k (mV)	$\tau_{\text{activation (-10mV)}}$(ms)[4)]	$\tau_{\text{activation (10mV)}}$(ms)[5)]
Vector	−72.7 ± 28.3 (7)	−5.1 ± 0.2 (9)	10.5 ± 0.9 (9)	1.53 ± 0.12 (15)	0.56 ± 0.03 (15)
RIM1α	−63.5 ± 15.4 (11)	−4.9 ± 0.3 (7)	9.6 ± 1.3 (7)	1.54 ± 0.05 (6)	0.71 ± 0.05 (6)*
RIM2α	−86.1 ± 33.4 (7)	−4.9 ± 0.3 (5)	9.6 ± 1.3 (5)	1.43 ± 0.18 (6)	0.51 ± 0.04 (6)
RIM3γ	−68.0 ± 8.0 (12)	−5.4 ± 0.3 (10)	7.4 ± 1.3 (10)	2.16 ± 0.20 (7)*	0.71 ± 0.06 (7)*
RIM4γ	−84.9 ± 12.6 (9)	−5.1 ± 0.2 (12)	8.6 ± 1.1 (12)	2.58 ± 0.27 (10)***	0.87 ± 0.02 (10)***

1) $*P < 0.05$, $***P < 0.001$ versus vector.

2) Numbers of cells analyzed are indicated in the parenthesis.

3) Ba^{2+} currents evoked by depolarizing pulse to 0 mV from a V_h of −100 mV are divided by capacitance.

4) Activation time constants obtained from currents elicited by 5-ms test pulse to −10 mV. The activation phases are well fitted by a single exponential function.

5) Activation time constants obtained from currents elicited by 5-ms test pulse to 10 mV.

Table S4 Effects of RIM siRNA applications on inactivation properties of VDCC in PC12 cells[1) 2) 3)].

siRNA	Inactivation parameters						
	a	$V_{0.5}^{Low}$ (mV)	K^{Low} (mV)	*b*	$V_{0.5}^{High}$ (mV)	K^{High} (mV)	1–*a*–*b*
siControl	0.21 ± 0.04 (7)$^{\#\dagger}$	−35.2 ± 2.1 (7)	−8.3 ± 1.3 (7)	0.36 ± 0.03 (7)	−4.5 ± 1.2 (7)	−4.0 ± 0.4 (7)	0.42 ± 0.02 (7)$^{\#\dagger\dagger\dagger}$
siRIM1&2	0.35 ± 0.04 (9)*	−37.6 ± 1.9 (9)	−8.7 ± 0.6 (9)	0.31 ± 0.02 (9)	−5.7 ± 1.5 (9)	−4.6 ± 0.8 (9)	0.30 ± 0.04 (9)*
siRIM3&4	0.38 ± 0.02 (6)*	−40.1 ± 2.0 (6)	−8.9 ± 0.9 (6)	0.36 ± 0.01 (6)	−1.8 ± 2.1 (6)	−6.1 ± 1.0 (6)*	0.26 ± 0.03 (6)***
siRIM1&2&3&4	0.46 ± 0.04 (8)***$^{\#\dagger}$	−38.9 ± 1.9 (8)	−8.5 ± 0.7 (8)	0.38 ± 0.05 (8)	−4.8 ± 0.9 (8)	−5.2 ± 0.8 (8)	0.17 ± 0.02 (8)***$^{\#\#\#\dagger\dagger\dagger}$
siRIM1&2 + RIM1*&2*	0.05 ± 0.02 (9)**$^{\#\#\#\dagger\dagger\dagger}$	–40.4 ± 2.3 (9)	–6.6 ± 0.1 (9)	0.54 ± 0.02 (9)*$^{\#\#\#\dagger\dagger}$	–3.7 ± 0.9 (9)	–4.4 ± 0.25 (9)$^{\#}$	0.41 ± 0.01 (9)$^{\#\dagger\dagger\dagger}$
siRIM3&4 + RIM3*&4*	0.12 ± 0.05 (7)$^{\#\#\#\dagger\dagger\dagger}$	–36.3 ± 4.9 (7)	–9.3 ± 0.6 (7)	0.47 ± 0.05 (7)$^{\#\#}$	–3.4 ± 1.2 (7)	–3.9 ± 0.7 (7)$^{\#}$	0.42 ± 0.05 (7)$^{\#\dagger\dagger\dagger}$

1) *P < 0.05, **P < 0.01, ***P < 0.001 versus siControl.

2) $^{\#}P$ < 0.05, $^{\#\#}P$ < 0.01, $^{\#\#\#}P$ < 0.001 versus siRIM1&2

3) $^{\dagger}P$ < 0.05, $^{\dagger\dagger}P$ < 0.01, $^{\dagger\dagger\dagger}P$ < 0.001 versus siRIM3&4.

4) Numbers of cells analyzed are indicated in the parenthesis.

Table S5 Effects of RIM siRNA applications on activation properties of VDCC in PC12 cells[1)].

siRNA	Current density (pA / pF)[2)]	Activation parameters	
		$\tau_{activation\ (-10mV)}$(ms)[3)]	$\tau_{activation\ (10mV)}$(ms)[4)]
siControl	−29.6 ± 2.1 (12)	1.26 ± 0.22 (6)	0.95 ± 0.16 (6)
siRIM1&2	−31.1 ± 3.7 (17)	1.49 ± 0.16 (12)	0.75 ± 0.08 (12)
siRIM3&4	−26.9 ± 2.4 (21)	1.32 ± 0.16 (12)	0.73 ± 0.05 (12)
siRIM1&2&3&4	−27.6 ± 2.8 (27)	1.64 ± 0.10 (12)	0.87 ± 0.05 (12)
siRIM1&2 + RIM1*&2*	−21.6 ± 3.8 (11)	1.48 ± 0.10 (11)	0.95 ± 0.10 (11)
siRIM3&4 + RIM3*&4*	−20.9 ± 2.7 (8)	1.74 ± 0.18 (8)	1.03 ± 0.10 (8)

1) Numbers of cells analyzed are indicated in the parenthesis.

2) Ba^{2+} currents evoked by depolarizing pulse to 0 mV from a V_h of –80 mV are divided by capacitance.

3) Activation time constants obtained from currents elicited by 30-ms test pulse to –10 mV. The activation phases are well fitted by a single exponential function.

4) Activation time constants obtained from currents elicited by 30-ms test pulse to 10 mV.